Delft University of Technology

Evolution and role of vacancy clusters at grain boundaries of ZnO:Al during accelerated degradation of Cu(In, Ga)Se2 solar cells revealed by positron annihilation

Shi, Wenqin; Theelen, Mirjam; Illiberi, Andrea; van der Sar, Stefan; Butterling, Maik; Schut, Henk; Zeman, Miro; Brück, Ekkes; Eijt, Stephan; More Authors

Publication date
2018

Document Version
Final published version

Published in
Physical Review Materials

Citation (APA)
Shi, W., Theelen, M., Illiberi, A., van der Sar, S., Butterling, M., Schut, H., Zeman, M., Brück, E., Eijt, S., & More Authors (2018). Evolution and role of vacancy clusters at grain boundaries of ZnO:Al during accelerated degradation of Cu(In, Ga)Se2 solar cells revealed by positron annihilation. *Physical Review Materials*, *2*, 1-18. Article 105403.

Important note
To cite this publication, please use the final published version (if applicable).
Please check the document version above.

Copyright
Other than for strictly personal use, it is not permitted to download, forward or distribute the text or part of it, without the consent of the author(s) and/or copyright holder(s), unless the work is under an open content license such as Creative Commons.

Takedown policy
Please contact us and provide details if you believe this document breaches copyrights.
We will remove access to the work immediately and investigate your claim.

This work is downloaded from Delft University of Technology.
For technical reasons the number of authors shown on this cover page is limited to a maximum of 10.

Evolution and role of vacancy clusters at grain boundaries of ZnO:Al during accelerated degradation of Cu(In, Ga)Se_2 solar cells revealed by positron annihilation

Wenqin Shi,[1] Mirjam Theelen,[2] Andrea Illiberi,[2] Nicolas Barreau,[3] Stefan J. van der Sar,[1] Maik Butterling,[1,4] Henk Schut,[4] Werner Egger,[5] Marcel Dickmann,[6] Christoph Hugenschmidt,[6] Miro Zeman,[7] Ekkes Brück,[1] and Stephan W. H. Eijt[1,*]

[1]*Fundamental Aspects of Materials and Energy, Faculty of Applied Sciences, Delft University of Technology, Mekelweg 15, NL-2629 JB Delft, Netherlands*

[2]*TNO/Solliance, Thin Film Technology, High Tech Campus 21, NL-5656 AE Eindhoven, Netherlands*

[3]*Institut des Matériaux Jean Rouxel (IMN)-UMR 6502, Université de Nantes, CNRS, 2 rue de la Houssinière, BP 32229, F-44322 Nantes Cedex 3, France*

[4]*Neutron and Positron Methods in Materials, Faculty of Applied Sciences, Delft University of Technology, Mekelweg 15, NL-2629 JB Delft, Netherlands*

[5]*Institut für Angewandte Physik und Messtechnik, Universität der Bundeswehr München, D-85579 Neubiberg, Germany*

[6]*Physics Department and Heinz Maier-Leibnitz Zentrum (MLZ), Technische Universität München, D-85748 Garching, Germany*

[7]*Photovoltaic Materials and Devices, Faculty of Electrical Engineering, Mathematics, and Computer Science, Delft University of Technology, Mekelweg 4, NL-2628 CD Delft, Netherlands*

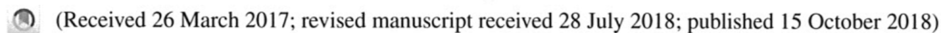
(Received 26 March 2017; revised manuscript received 28 July 2018; published 15 October 2018)

Positron annihilation lifetime spectroscopy (PALS) and Doppler broadening positron annihilation spectroscopy (DB-PAS) depth profiling demonstrate pronounced growth of vacancy clusters at the grain boundaries of as-deposited Al-doped ZnO films deposited as transparent conductive oxide (TCO) on Cu(In, Ga)Se_2 (CIGS) solar cells upon accelerated degradation at 85 °C/85% relative humidity. Quantitative fractions of positrons trapped either in the vacancy clusters at the grain boundaries or in Zn monovacancies inside the grains of ZnO:Al were obtained by detailed analysis of the PALS data using a positron trapping model. The time and depth dependence of the positron Doppler depth profiles can be accurately described using a planar diffusion model, with an extracted diffusion coefficient of 35 nm^2/hour characteristic for in-diffusion of molecules such as H_2O and CO_2 into ZnO:Al TCO films via the grain boundaries, where they react with the ZnO:Al. This leads to increased open volume at the grain boundaries that imposes additional transport barriers and may lead to charge carrier trapping and nonradiative recombination. Simultaneously, a pronounced increase in series resistance and a strong reduction in efficiency of the ZnO:Al capped CIGS solar cells is observed on a remarkably similar timescale. This strongly indicates that these atomic-scale processes of molecular in-diffusion and creation of open volume at the grain boundaries play a key role in the degradation of the solar cells.

PhySH: Solar Cells, Positron Annihilation Spectroscopy, Grain Boundaries, Vacancies, Thin Films, Diffusion, Electrical Properties, Solid State Chemistry, Optoelectronics

DOI: 10.1103/PhysRevMaterials.2.105403

I. INTRODUCTION

Thin-film Cu(In, Ga)Se_2 (CIGS) solar cells are promising in view of their high efficiency and low cost. Research-cell efficiencies have reached 22.6% for a CIGS cell [1], currently the highest efficiency for thin-film solar cells employing a single absorber layer, besides (expensive) III-V based solar cells. Recently reported progress in high-efficiency CIGS cells using, e.g., alkali postdeposition treatment [2] or alternative buffer layers [3] [Zn(O,S)] leads to high expectations for expanding the commercial application of CIGS solar cells. Nevertheless, stability issues are still drawing considerable attention, since larger-scale commercial introduction of CIGS photovoltaic (PV) technology requires cheap and highly efficient modules with long and predictable lifetimes. Unfortunately, knowledge about the lifetime of CIGS modules is still limited, which is reflected in the results of field studies: degradation rates varying from nearly 0 to approximately 4 percent per year were observed [4–7]. Therefore, considerable costs are made for reliable package materials, which are especially high for flexible modules. These costs can be reduced by more intrinsically stable solar cells. Clearly, environmental degradation of CIGS solar cells needs to be prevented, making the identification of the degradation mechanisms of CIGS solar cells a crucial aspect in their development.

A key component of CIGS solar cells is the transparent conducting oxide (TCO) electrode. Al-doped ZnO (ZnO:Al) is a very promising TCO for photovoltaic cells because of its good optoelectronic properties, which include both high transparency and high electrical conductivity simultaneously. Furthermore, ZnO:Al consists of elements with a high abundancy and is a cheap material. However, ZnO:Al as the TCO window material of CIGS solar cells is notably sensitive to moisture [7]. When exposed to accelerated damp-heat (DH) testing, the optical properties of ZnO:Al exhibit only minor

*Corresponding author: s.w.h.eijt@tudelft.nl

 ©2018 American Physical Society

changes, mainly in the infrared region by degradation-induced changes in the charge carrier densities. However, its electrical properties deteriorate significantly [8]. This can be attributed to the decreased charge carrier concentrations [9] and reduced mobility of minority charge carriers [8,9], caused by an increase in the concentration of scattering centers and changes in the potential barriers at the grain boundaries of the ZnO:Al layer [8,9]. Insights into the electronic and atomic-scale structure of grain boundaries of Cu(In, Ga)Se_2 thin film absorber layers is crucial for the development of CIGS solar cells as well, in order to reveal the nature of the influence of the grain boundaries in CIGS on charge carrier transport [10,11]. These grain boundaries also play an important role in understanding the in-diffusion of Na^+ (and K^+) into the Cu(In, Ga)Se_2 and CdS layers of CIGS solar cells, a key process in the formation of optimized CIGS/CdS heterojunctions required to achieve very high solar cell efficiencies [12]. Although quite a few studies have been performed to monitor the degradation of ZnO:Al TCO films, few characterization techniques can detect the impact of degradation on the nanoscale properties of ZnO:Al film directly. For example, UV-VIS optical reflection-transmission spectroscopy hardly detects any change in the optical spectra in the UV and visible range after degradation. A recent x-ray diffraction (XRD) study reveals a pronounced increase in the compressive in-plane stress, which can be attributed to the in-diffusion of molecules and stress buildup due to the subsequent chemical reactions in the grain boundaries [13]. Nevertheless, it provides an indirect view on the possible mechanism of degradation.

In this study, we apply positron annihilation as a proven depth-sensitive technique [14] in order to examine the depth-resolved changes resulting from damp-heat degradation of unpackaged ZnO:Al/i-ZnO/CdS/CIGS/Mo solar cells deposited on soda lime glass at 85 °C/85% relative humidity (RH). Positron annihilation spectroscopy is an effective way to probe point defects, and is in particular sensitive to the presence of neutral and negatively charged vacancies [15]. Positron annihilation lifetime spectroscopy (PALS) has a proven sensitivity to determine vacancy concentrations in the range of about 10^{-6} to 10^{-4}, depending on the type of material [15,16]. Point defects are known to have an important effect on the electronic and optoelectronic properties of ZnO. For example, Zn vacancies act as the dominant type of compensating acceptor in Al-doped ZnO [17,18]. Also, hydrogen may bind to oxygen and form shallow donor complexes in ZnO [19]. Positron annihilation has been used extensively to clarify the nature of vacancy-related defects and hydrogen-vacancy interactions in ZnO and their relationship with the microelectronic and optoelectronic properties of ZnO and ZnO-based devices [20–24].

Clearly, in order to gain a better understanding of the degradation mechanism of CIGS cells, it is important to identify and quantify the presence and evolution of such point defects in the ZnO:Al layer. Depending on their kinetic energy, positrons can reach the various individual layers in a CIGS solar cell and provide detailed insights into the defect properties of each individual layer separately, including the ZnO:Al TCO and CIGS absorber layer. In this study, we show that positrons trap and annihilate inside grains as well as at grain boundaries of the ZnO:Al layer. The corresponding positron lifetimes and Doppler broadening momentum distributions provide key information on the growth of open volume defects in the grains and at the grain boundaries, resulting from the accelerated degradation by exposure to moisture and heat. In particular, the type and concentration of vacancy-related defects and their evolution in the ZnO:Al layer during the degradation process were determined by the positron annihilation lifetime spectroscopy (PALS) and Doppler broadening positron annihilation spectroscopy (DB-PAS) methods, providing important insights into the mechanisms of the degradation in optoelectronic properties of CIGS solar cells using Al-doped ZnO:Al as TCO by damp-heat (DH) accelerated degradation.

II. EXPERIMENTAL

The unpackaged CIGS solar cells consisted of a multilayer of aluminium-doped zinc oxide (ZnO:Al)/intrinsic zinc oxide (i-ZnO)/cadmium sulphide (CdS)/Cu(In, Ga)Se_2 (CIGS)/molybdenum (Mo) on soda lime glass (SLG), with an additional Ag front contact and an additional Ag back contact on the Mo film for the devices used in the photocurrent-voltage (*I-V*) solar cell characterization. The CIGS absorber layer (with an average thickness of 2.6 μm) was produced by 3-stage coevaporation at a maximum deposition temperature of 580 °C, using a synthesis procedure very similar to the one described in [25]. The CdS layer (with a thickness of 50 nm) was synthesized using chemical bath deposition (CBD). The ZnO:Al and i-ZnO layers (with a thickness of 220 nm and 50 nm, respectively) were produced by RF sputtering, using 2 wt. % Al_2O_3 for the synthesis of the ZnO:Al layer. The thickness of the Mo coating of the SLG glass was 650 nm. A schematic of the ZnO:Al/i-ZnO/CdS/CIGS/Mo/SLG layer composition of the investigated solar cells is presented (without Ag contacts) in Fig. 1. Nine samples with a size of about 1.25 cm × 1.5 cm, sawn from a single 2.5 cm × 7.5 cm CIGS solar cell slide produced in Nantes, were degraded simultaneously by exposure to 85 °C/85% RH heat-moisture conditions in a damp-heat chamber during various time intervals, with a maximum total degradation time of 1218 hours. According to International Electrotechnical Commission (IEC) standard 61646, 1000 hours of exposure to these conditions should mimic 25 years of field exposure in Miami (it should be

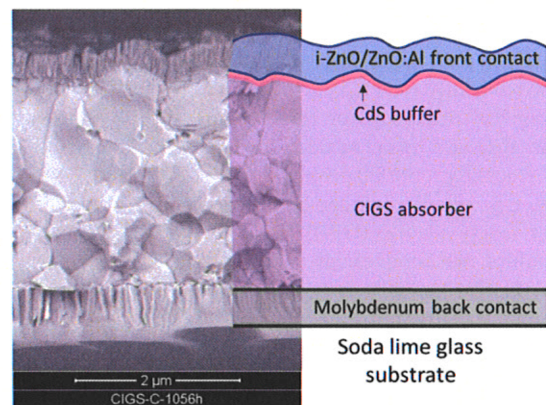

FIG. 1. Schematic representation of the ZnO:Al/i-ZnO/CdS/CIGS/Mo/SLG layer composition of the CIGS solar cells merged with a representative SEM image.

TABLE I. Current density–voltage (J-V) parameters for as-prepared CIGS solar cells under AM1.5 illumination (error bars correspond to 1 standard deviation derived from measured values for 9 samples).

CIGS solar cells	η (%)	FF (%)	V_{OC} (mV)	J_{SC} (mA/cm^2)	R_s (ohmscm^2)	R_{sh} (ohmscm^2)
as-deposited	14.0 ± 0.3	72.1 ± 0.3	604 ± 5	32.3 ± 0.5	2.2 ± 0.1	840 ± 20
683-hour degradation	5.3 ± 0.3	38 ± 2	537 ± 4	26 ± 2	12 ± 2	88 ± 20

noted here that the exact correspondence between accelerated degradation and field testing is topic of debate). Each sample was used to produce a 9×9 mm^2 sample for the positron annihilation measurements and 3×3 mm^2 samples, with a surface area of 8mm^2 effectively available for optical illumination after the Ag contact was established, for the solar cell device characterization. The differences in the solar cell parameters (V_{OC}, J_{SC}, FF, η), obtained under standard AM1.5 illumination conditions, among 9 samples degraded at the same conditions were not statistically significant (see Table I for the averaged values). This verifies that the samples sawn from the single large solar cell slide were rather uniform, and their degradation behavior at different time intervals can be directly compared. As described in Ref. [26], I-V measurements were performed by a Keithley 2440 5A source meter, with the data collection system positioned outside the damp-heat chamber. The series and shunt resistance of the solar cell were determined by the definition of the slope of the I-V curves. After each degradation step at Solliance/TNO Eindhoven, the samples without Ag electrodes were sealed and sent to Delft University of Technology for the positron annihilation measurements. The samples were stored in an Ar-filled glovebox when they were not measured.

Doppler broadening positron annihilation spectroscopy (DB-PAS) measurements were performed at room temperature using the monoenergetic positron beam VEP. The implantation energy of positrons was varied from 0.1 keV to 25 keV. The intensity of the low-energy positron beam at sample position is around 10^4 e^+/s, and the FWHM size of the beam is 7 mm in diameter [27]. A liquid-nitrogen-cooled high-purity Ge (HPGe) detector with an energy resolution of 1.3 keV was used to determine the energy of the emitted annihilation γ rays. The Doppler broadening of the photopeak is determined by the electron momentum distributions $N^{2\gamma}(p)$ as seen by the annihilating positrons. S and W parameters were extracted from the measured Doppler broadened annihilation γ-ray photopeak, defined as the fraction of counts in the central region and in the wing regions of the 511 keV annihilation photopeak [$N^{2\gamma}(p)$], respectively. The momentum windows used to deduce the S parameter and W parameter are $|p_L| < 0.41$ a.u. (1a.u. $= 7.2974 \times 10^{-3} m_0 c$) and 1.12au. $< p_L <$ 3.21a.u., respectively, with longitudinal momentum $p_L = 2\Delta E/c$ and ΔE the Doppler shift in energy of the detected annihilation γ ray. The S parameter is a measure of positron annihilation with valence electrons, which provides sensitivity to the electronic structure and the presence of open volume defects such as vacancies or vacancy clusters [16,28,29]. The increase in concentration or size of vacancies or vacancy clusters in an otherwise identical material generally leads to an increase of the S parameter. The W parameter is a measure of annihilation with (semi)core electrons which provides chemical sensitivity to the positron trapping site [16,28,29]. The S-parameter depth profiles were analyzed using the VEPFIT program, which solves the full positron implantation-diffusion problem for a system of layers and calculated $S(E)$ curves are fitted to the experimental data, with the S parameter of the respective layer, its thickness, and the positron diffusion length for each layer with a given mass density as fit parameters. Makhovian implantation profiles were assumed with an average implantation depth (in nm) according to $z_{ave} = \alpha_p E^n / \rho$, with the positron implantation energy E in keV, the empirical value for the exponent set at $n = 1.62$, $\alpha_p = 4.0 \mu\text{gcm}^{-2}$ keV$^{-1.62}$, and the density ρ in g/cm^3 [28].

Coincident Doppler broadening (CDB) was used to determine the electron-positron momentum distributions $N^{2\gamma}(p)$ at higher momentum resolution and significantly reduced background. The CDB measurements were performed using the intense reactor-based low-energy positron beam POSH. The intensity of the POSH beam is around 1×10^8 e^+/s, and the positron implantation energy can be varied between 0.1 keV and 13.5 keV [30]. Two collinear HPGe detectors were used to increase the peak-to-background ratio in the electron-positron momentum distributions collected at an energy resolution of 0.9 keV in the CDB experiments. At each selected positron implantation energy, 10^7 counts of positron annihilation events were collected. The 1D electron-positron momentum distributions obtained from the CDB measurements were normalized to the reference 1D electron-positron momentum distribution obtained for a hydrothermal (HT) grown ZnO single crystal (Mateck GmbH) at a positron implantation energy of 12 keV.

The CIGS solar cells were further examined in positron annihilation lifetime spectroscopy (PALS) studies using the pulsed low-energy positron lifetime spectrometer (PLEPS) instrument [31] of the neutron induced positron source (NEPOMUC) facility [32] at the Heinz Maier-Leibnitz Zentrum (MLZ) research reactor in Garching. Measurements on the CIGS solar cells were performed at selected positron energies between 1 and 18 keV. Around 4×10^6 counts were collected for each lifetime spectrum. The lifetime spectra were fitted by using the LT program [33].

The morphology and grain size of as-deposited and degraded (1056 h) ZnO:Al films was determined by scanning electron microscopy using a Nova NanoSEM 650 (FEI) microscope at TNO-Rijswijk.

III. RESULTS AND DISCUSSION

A. Time dependence of accelerated degradation of CIGS solar cells

Figure 2(a) shows the evolution of the current density–voltage (J-V) curves, determined under AM1.5 illumination,

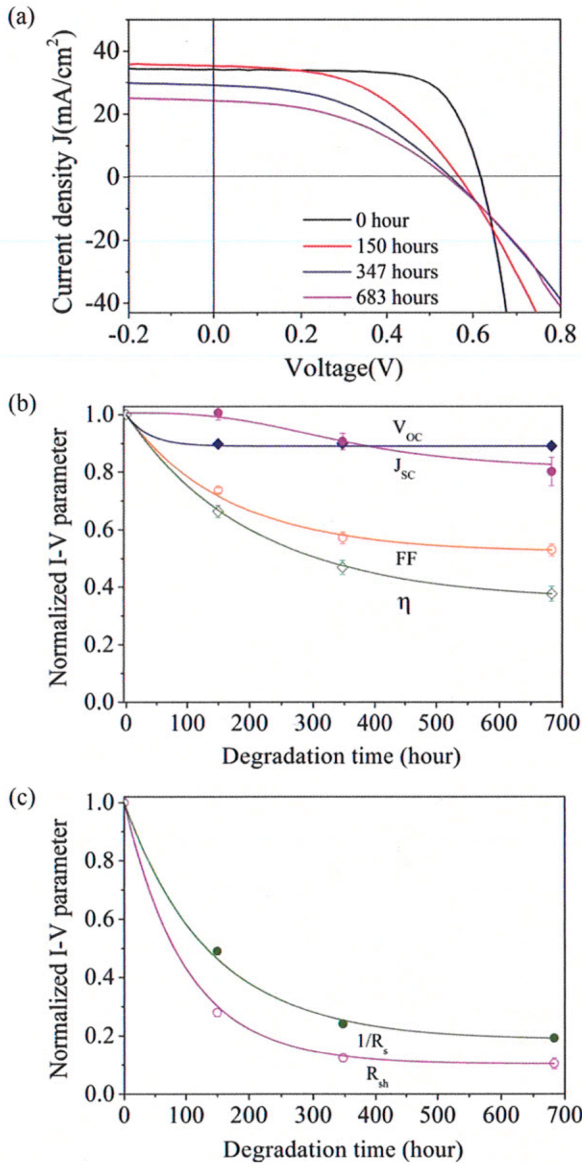

FIG. 2. (a) Current density–voltage (*J-V*) curves at AM1.5 illumination of CIGS solar cells degraded from 0 h to 683 h at 85 °C/85% RH. (b) CIGS solar cell parameters as a function of damp-heat degradation time, normalized to the parameters for the as-deposited state: open circuit voltage, V_{OC} (blue solid diamonds); short circuit current density, J_{SC} (magenta solid circles); fill factor, *FF* (orange open circles); efficiency, η (green open diamonds). (c) Shunt resistance, R_{sh} (magenta open circles), and inverse of the series resistance, $1/R_s$ (green solid circles), as a function of damp-heat degradation time, normalized to the parameters for the as-deposited state.

of unpackaged CIGS solar cell devices as a function of accelerated degradation time of up to 683 hours of exposure to temperature-moisture conditions of 85 °C/85% RH. The corresponding time dependence of the solar cell parameters, as extracted from the *J-V* curves and normalized to those of the as-deposited CIGS solar cells, is shown in Figs. 2(b) and 2(c), including the solar cell efficiency (η), fill factor (*FF*), open circuit voltage (V_{OC}), short circuit current (J_{SC}), series resistance (R_S), and shunt resistance (R_{sh}). The efficiency of the CIGS solar cells decreases substantially from 14.0% in the as-prepared state to 5.3% after a degradation time of 683 h, demonstrating that substantial degradation takes place on this timescale. Clearly, a major drop in fill factor occurs, in parallel to a large increase in series resistance (R_S) and a fast decrease in shunt resistance (R_{sh}). On the other hand, the open circuit voltage V_{OC} and open circuit current J_{SC} show more moderate decreases of 11% and 20%, respectively. Thus, the fill factor *FF* is the dominant factor in the decrease in solar cell efficiency, and is in its turn largely affected by both R_S and R_{sh}. The series resistance relates to the transport of current through the semiconductor layers and interfaces of the ZnO:Al/i-ZnO/CdS/CIGS multilayer device, and through the contacts with the Mo film and Ag electrodes. In particular, it is known that the series resistance is very sensitive to changes in the ZnO:Al TCO layer, making it a key factor in the degradation of CIGS solar cells employing Al-doped ZnO as TCO. In order to determine key aspects of the nanoscale mechanism of degradation, detailed insights into the layer-resolved defect evolution in the ZnO:Al/i-ZnO/CdS/CIGS thin film solar cells is gained by employing depth-sensitive positron annihilation methods, as described in the next sections.

B. Doppler Broadening depth profiles of as-deposited and degraded CIGS solar cells with a ZnO:Al TCO top layer

In order to examine which parts of the CIGS solar cell are degraded during the damp-heat treatment, we first used positron Doppler broadening depth profiling to monitor the ZnO:Al/i-ZnO/CdS/CIGS/Mo samples as a function of degradation time at 85 °C and 85% RH (Fig. 3). The *S* parameter of the as-deposited sample shows a rapid decrease as a function of positron implantation energy in the low energy range up to about 1.5 keV [Fig. 2(a)] due to (1) annihilation of epithermal (i.e., nonthermalized) positrons [28] and (2) the decrease in fraction of positrons (with increased implantation energy) that, after implantation and thermalization in the subsurface region, are able to diffuse back and annihilate at the surface [28]. Correspondingly, a rather short *effective* positron diffusion length of $L_+ = 2 \pm 1$ nm was extracted by VEPFIT analysis [28] of the *S*(*E*) and *W*(*E*) depth profiles. Subsequently, a plateau is reached where positrons probe the Al-doped ZnO TCO layer, after which the *S* parameter increases gradually up to the highest positron implantation energy of 25 keV where positrons primarily are stopped and annihilate in the CIGS absorber layer, corresponding to an average positron implantation depth of about 1.1 μm. The Mo metal electrode layer underneath the CIGS absorber layer was situated at too large depth below the surface of the solar cell and could thus not be detected. The dependence of the *W* parameter on positron implantation energy shows a similar, mirrored pattern [Fig. 3(b)].

The depth profiles of the as-deposited sample could be fitted using VEPFIT analysis with three layers, ZnO:Al, CdS, and CIGS (Table II and Fig. 4). The presence of the thin intermediate CdS buffer layer was hidden and was not revealed in the positron depth profiles, since its characteristic *S* and

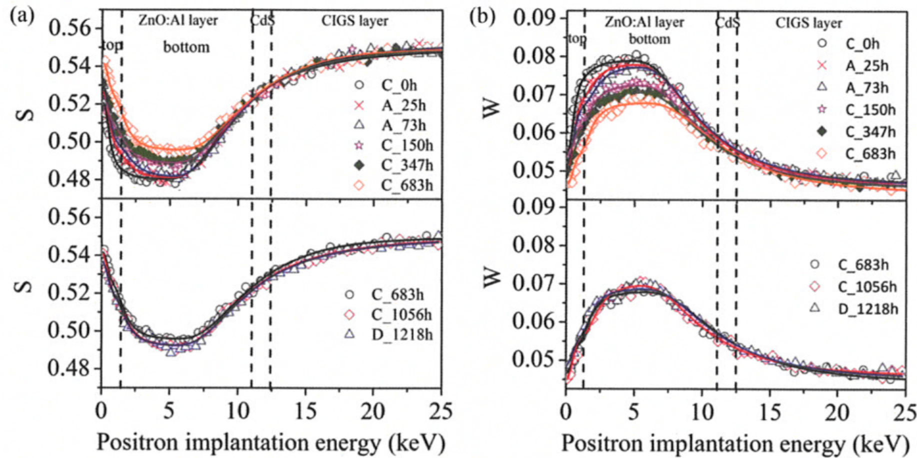

FIG. 3. (a) Doppler S parameter as a function of positron implantation energy for CIGS solar cells at various degradation times at 85 °C/85% RH. Symbols are experimental data and solid lines are fit curves obtained by VEPFIT analysis employing a 4-layer model (3 layers for the as-deposited state). (b) Doppler W parameter as a function of positron implantation energy for CIGS solar cells at various degradation times at 85 °C/85% RH.

W parameter are in between those of ZnO:Al and CIGS, as determined for other samples where the ZnO:Al TCO was not deposited and the CdS layer formed the top layer. The presence of the CdS buffer layer was experimentally verified by Raman spectroscopy using an Ar ion laser at 514.5 nm, since the Raman spectra were dominated by the characteristic wurtzite CdS LO peaks at 302 cm^{-1} and 605 cm^{-1}. The parameters for the CdS layer are given in Table II and were kept constant in the VEPFIT analysis. In the VEPFIT model, the ~50 nm i-ZnO layer was included as a part of the bottom ZnO:Al layer, assuming the same S and W parameters as the bottom ZnO:Al layer both in the as-prepared state and during the degradation process. Table II provides an overview of the best-fit parameters for the three layers. The fractions of positrons annihilating in each layer of the as-deposited CIGS solar cell, extracted using VEPFIT analysis, are shown in Fig. 4 as a function of positron implantation energy.

Figure 3 shows that the degradation leads to pronounced changes in the S and W parameters at low positron implantation energies. The S parameter shows a strong increase already for relatively short degradation times of 25 and 73 h in the low-energy range up to 4 keV. The rise in S parameter continues for longer degradation times up to 683 h, extending towards increasingly higher positron implantation energies of up to at least 8 keV. This indicates that the nanostructural changes of the ZnO:Al layer occur at increasingly large depths below the surface with prolonged degradation time, consistent with an in-diffusion mechanism in which in-diffusion of atmospheric molecules such as H_2O and CO_2 plays a key role [8,26]. A saturation of the S and W of the ZnO:Al layer seems to set in for longer degradation times beyond 683 h. As shown in Fig. 3, there is no visible change in the CIGS absorber layer, while the accelerated degradation affects the ZnO:Al layer substantially. This result is consistent with previous research [8,26], which indicated that the CIGS solar cell degradation mechanism induced by damp-heat exposure can be mainly attributed to the degradation of ZnO:Al TCO and the Mo metal back contact. The increase in S and decrease in W suggest that the degradation of the ZnO layer involves the formation of open volume, such as monovacancies or small vacancy clusters. Namely, trapping of positrons in neutral or negatively charged vacancies leads to less overlap with core electrons, while valence electron orbitals of the surrounding atoms extend farther into the open space where the positron resides. The resulting higher fraction of annihilation with valence electrons leads to the detected increase in the S parameter. Also, the S parameter of the surface is seen to increase, which is expected in view of the large changes that start at the surface and in time affect a substantial part of the ZnO:Al layer.

In order to gain a better insight into the nature of the observed changes in the Doppler depth profiles and the evolution of the involved defect structures during the degradation process, we first employed a conventional approach to the analysis of the depth profiles, assuming a layered model within VEPFIT. Once degradation had started, a satisfactory analysis of the depth profiles of the degraded samples could only be obtained using four layers instead of three layers, as

TABLE II. VEPFIT analysis best-fit parameters for as-deposited CIGS solar cell using a 3-layer model.

Layer	Density (g/cm^3)	L_+ (nm)	Layer width (nm)	S parameter	W parameter
ZnO:Al	5.606	2	257	0.482 ± 0.0002	0.078 ± 0.001
CdS	4.83	2	18	0.554 ± 0.0003	0.041 ± 0.001
CIGS	5.7	2	∞	0.550 ± 0.0003	0.046 ± 0.001

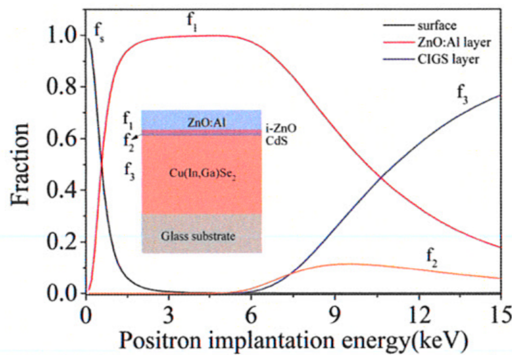

FIG. 4. Fraction of positrons that annihilate in each layer of the as-deposited ZnO:Al/CIGS solar cell as a function of positron implantation energy, extracted from the VEPFIT program: f_s, surface; f_1, ZnO:Al/i-ZnO, f_2, CdS; f_3, CIGS.

was immediately visible by eye judged from the comparison of experimental and fit curves, confirmed by the strong difference in χ^2 parameter obtained from the VEPFIT analysis using either three or four layers in the model. Now, two layers (a top layer and a bottom layer) were required to fit the Al-doped ZnO TCO layer satisfactorily, and further a thin CdS buffer layer and the CIGS layer were included. Figure 5 presents the extracted evolution of S and W parameters in the top ZnO:Al layer with a thickness of 20 ± 3 nm and in the bottom layer of ZnO:Al (260 ± 15 nm) as a function of degradation time. At the start of the degradation process, the S parameter of the top layer increases rapidly while the S parameter of the bottom layer still stays constant and starts to increase only after a delay of about 50–100 h. This delay points to a direct connection to the diffusion process which has been proposed as the primary cause for the solar cell degradation, involving molecules such as H_2O and CO_2 from the atmospheric environment in the DH chamber that penetrate and diffuse into the layer, starting from the surface [8]. Furthermore, Fig. 5 shows that the S and W parameters in both the top and bottom layers level off for degradation times beyond about 400 hours, indicating that the nanostructural changes of the ZnO:Al TCO layer occur on a timescale similar to the decay of the solar parameters such as solar cell efficiency and series resistance (Fig. 1). This suggests a direct relationship between the in-diffusion of environmental gas molecules leading to solar cell degradation and the formation of additional open volume defects such as vacancies or vacancy clusters in the ZnO:Al top and bottom layers as a result of the damp-heat accelerated degradation treatment. In the next section, we therefore present a way to analyze the depth and time dependence of the positron Doppler depth profiles based on a direct connection to the in-diffusion process.

For completeness, in order to examine whether the observed changes could alternatively be primarily due to changes at the surface of the sample, we analyzed the S parameter depth profiles using two alternative models [34]. The analysis shows that both of these models can be disregarded, however, either (1) because of failure to provide satisfactory fits to the Doppler depth profiles (model S1), or (2) the model leads to parameters inconsistent with the evolution of defects in the ZnO:Al (model S2). Noteworthy, model S2 shows that surface annihilation contributes to at most a (very) minor fraction in the range of positron implantation energies of 2–8 keV [34]. Figure 4 shows that at 1 keV surface annihilation contributes only ~10% to the positron annihilation, and consequently the variation in surface annihilation cannot explain the large changes observed in the range from ~1 keV and beyond.

C. Diffusion model analysis of the degradation-induced changes in the Doppler-broadening depth profiles

In order to examine whether the evolution of the Doppler depth profiles is consistent with an in-diffusion mechanism as suggested by the evolution of the S and W parameters with degradation time, we apply in this section an in-diffusion model to fit the depth and time dependence of the changes in the $S(E)$ and $W(E)$ profiles caused by accelerated degradation of the CIGS solar cells. When exposed to 85 °C/85% RH conditions, atmospheric species such as H_2O and CO_2 diffuse into the ZnO:Al layer covering the remainder of the CIGS solar cell. The in-diffusion may occur through the grain boundaries of the ZnO:Al film, and also, possibly generated H^+ might diffuse into the bulk of the grains. The in-diffused molecules will chemically react with the ZnO:Al at the grain boundaries, leading to the local removal of atoms and to the creation of new phases such as $Zn(OH)_2$ and Zn-based

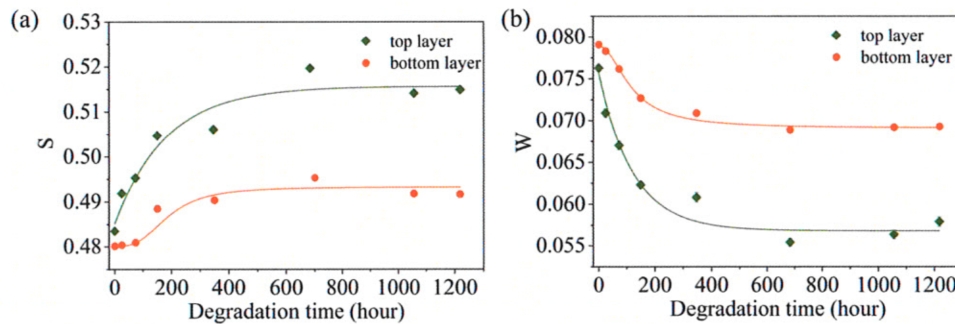

FIG. 5. (a) S and (b) W parameters as a function of the damp-heat degradation time for the 20 ± 3 nm ZnO:Al top layer and 260 ± 15 nm ZnO:Al bottom layer, respectively, obtained from VEPFIT analysis of Doppler S and W depth profiles.

carbonates which may exert a stress on the local environment [8,13]. These processes may therefore induce the formation of additional open volume at the grain boundaries as well as increase the size and/or concentration of vacancies inside the grains, respectively, as indicated from the Doppler broadening experiments by the increase in S parameter.

To the authors' knowledge, a model that takes into account the effect of a diffusion-related depth distribution of open volume defects on positron Doppler broadening depth profiles has not been reported in literature, and we describe the model in more detail in the Appendix. Briefly, in the diffusion model, it is assumed that the concentration of in-diffused atmospheric species is described by planar one-dimensional diffusion in a semi-infinite medium at a diffusion coefficient D that we assume to be constant over time and depth below the surface. The solution of the corresponding diffusion equation with concentration $C(0)$ at the surface can be expressed by an error function [35]:

$$C(z,t) = C(0)\left[1 - \mathrm{erf}\left(\frac{z}{2\sqrt{Dt}}\right)\right], \quad (1)$$

where $C(z,t)$ is the concentration as a function of depth z below the surface and t is the degradation time. In the model, we assume that the formation of additional open volume is proportional to the concentration of in-diffused molecules, and that the created open volume defects in turn lead to a proportional increase ΔS and decrease $|\Delta W| = -\Delta W$. In order to derive the dependence on positron implantation energy of $\Delta S(E)$ and $|\Delta W(E)|$, Makhovian distributions of order $m = 2$ for the positron implantation profiles were used, given by

$$P(z,E) = \frac{2z}{z_0^2} e^{-(z/z_0)^2}, \quad (2)$$

where $z_0 = 1.13 z_{\text{ave}}$ with the mean depth $z_{\text{ave}} = \alpha_p E^n/\rho$, ρ is the density of the ZnO:Al, and E is the positron implantation energy. In the analysis, the parameters $\alpha_p = 4.0 \mu\text{g}\,\text{cm}^{-2}\,\text{keV}^{-1.62}$ and $n = 1.62$ were used [28,36]. Diffusion of thermalized positrons is not taken into account in the model, which limits the validity of the model to the case where the positron diffusion length $L_+ \ll z_0$ [28,37], i.e., for films with moderate to high defect concentrations, or to sufficiently high positron implantation energies. In practice, back diffusion of thermalized positrons to the surface of the ZnO:Al TCO layer as well as epithermal positron annihilation is only appreciable for positron implantation energies $\leqslant$1.5 keV, indicating that the model can conveniently be applied at energies starting from ~1.5 keV as is included in our analysis implicitly, as explained further on.

One can thus derive that the dependence on positron implantation energy of the changes in the S and W parameters due to the degradation of the ZnO:Al TCO, $\Delta S_{\text{ZnO:Al}}(E,t)$ and $\Delta W_{\text{ZnO:Al}}(E,t)$, is described by (Appendix)

$$\Delta S_{\text{ZnO:Al}}(E,t) = \Delta S_0 \times \left[1 - e^{-(d/z_0)^2} - \int_0^d \mathrm{erf}\left(\frac{z}{2\sqrt{Dt}}\right)\frac{2z}{z_0^2}e^{-(z/z_0)^2}dz\right] \quad (3)$$

and

$$|\Delta W_{\text{ZnO:Al}}(E,t)| = \Delta W_0 \times \left[1 - e^{-(d/z_0)^2} - \int_0^d \mathrm{erf}\left(\frac{z}{2\sqrt{Dt}}\right)\frac{2z}{z_0^2}e^{-(z/z_0)^2}dz\right] \; (= -\Delta W), \quad (4)$$

with d the thickness of the ZnO:Al TCO layer. $\Delta S_0 = I_{\Delta S} \times C(0)$ and $\Delta W_0 = I_{\Delta W} \times C(0)$ are the change in S and W for annihilation of thermalized positrons inside the ZnO:Al just below the surface, with $I_{\Delta S}$ and $I_{\Delta W}$ intensity proportionality prefactors connecting ΔS_0 and ΔW_0 with the concentration of molecules at the surface $C(0)$. The cutoff at $z = d$ takes into account that at high positron implantation energies more and more positrons annihilate in the CdS and CIGS layers [28,37], that apparently are not affected by the in-diffusion of molecules. These positrons obviously do not probe the degradation-induced changes in the ZnO:Al layer.

The in-diffusion model was used in numerical simulations for the analysis of the observed changes $\Delta S_{\text{exp}}(E)$ and $-\Delta W_{\text{exp}}(E)$ in the Doppler depth profiles. Figure 6(a) presents the experimental curves for the change in S parameter $\Delta S_{\text{exp}}(E,t) - \Delta S_s(t) f_s(E)$ as a function of positron implantation energy, where $\Delta S_{\text{exp}}(E,t)$ is defined as the difference in the depth profile measured after degradation time t and that of the as-deposited state. Clearly, the S parameter of surface annihilation increases with degradation time $[\Delta S_s(t) > 0]$ due to the strong impact of the environmental exposure on the local composition and structure of the ZnO:Al outer surface (Fig. 3). The factor $\Delta S_s(t) f_s(E)$ accounts for the change in surface annihilation contribution at low positron implantation energies, in which the surface annihilation fraction $f_s(E)$ for the as-deposited sample determined by the VEPFIT analysis was used (Fig. 4). The contribution of surface annihilation was subtracted from $\Delta S_{\text{exp}}(E,t)$ to show separately the degradation-induced changes that occur in the ZnO:Al layer. The change in the S parameter for surface annihilation $\Delta S_s(t)$ was derived from the experimental values at the lowest positron implantation energies. The full curves in Fig. 6(a) represent best fits of the experimental data to numerically generated depth profiles $\Delta S_{\text{ZnO:Al}}(E,t)[1 - f_s(E)]$ of the in-diffusion model, where the factor $[1 - f_s(E)]$ used in the simulations takes into account the fraction of positrons that annihilate at the surface due to back diffusion of thermalized positrons and due to epithermal positrons, which starts to dominate in the low-energy subsurface range for energies below ~1.5 keV. The corresponding experimental and numerically generated depth profiles for $-\Delta W_{\text{ZnO:Al}}(E)[1 - f_s(E)]$ are given in Fig. 6(b). The same apparent diffusion coefficient D is used in the best-fit analysis of both S and W for all degradation times. Finally, Fig. 6(c) presents the degradation time dependence of $\Delta S_0(t) = I_{\Delta S}(t)C(0)$ and $\Delta W_0(t) = I_{\Delta W}(t)C(0)$ obtained from the analysis based on Eqs. (3) and (4).

Clearly, the in-diffusion model describes the experimental depth profiles satisfactorily, using only two independent parameters, the (apparent) diffusion coefficient D and ΔS_0 (or ΔW_0) for all degradation times in the range of 0–683 h. A good agreement with the experimental data as a function

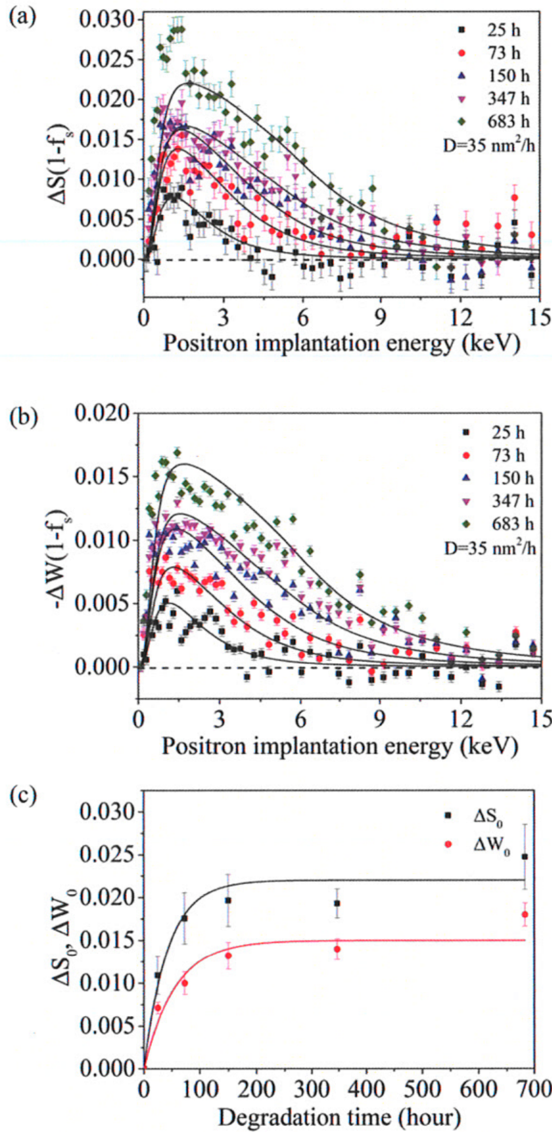

FIG. 6. Depth dependence of the change in Doppler depth profiles at various degradation times. (a) $\Delta S_{\mathrm{ZnO:Al}}(E)[1-f_s(E)]$. (b) $-\Delta W_{\mathrm{ZnO:Al}}(E)[1-f_s(E)]$. (c) Time dependence of ΔS_0 and ΔW_0 for the ZnO:Al layer, extracted using the in-diffusion model best-fit analysis [solid lines in panels (a) and (b)] described in the text and in the Appendix.

of degradation time could be obtained with a diffusion coefficient of $D = 35\ \mathrm{nm}^2/\mathrm{h}$. This reveals that the diffusion model provides a good description of the evolution of the S and W depth profiles with the degradation time. Furthermore, Fig. 6(c) shows that ΔS_0 and ΔW_0 depend in a very similar way on degradation time, providing further support to the validity of the model. Nevertheless, ΔS_0 and ΔW_0 are not constant in the initial phase up to ~200 h of degradation, in contrast to what would be expected if the change in S and W at depth z is directly proportional to the concentration of in-diffused molecules. This can be understood, since S and W not only depend on the concentration of in-diffused molecules, but also on the type of vacancy-related defects, in particular their size. The initial increase in ΔS_0 and ΔW_0 thus seems to reflect the growth in size of the vacancy clusters. This is indeed observed in the PALS experiment described in Sec. III E and is furthermore inferred from the evolution of the coincidence Dopper broadening momentum distributions described in Sec. III D for degradation times up to 150 h. The initial increase in ΔS_0 and ΔW_0 thus reflects the fact that the S and W parameters are a measure for the open volume created by the in-diffusion of molecules and release of local stress induced by chemical reactions, rather than a direct measure for the concentration of in-diffused molecules.

We note that for long degradation times, the model curves in Figs. 6(a) and 6(b) deviate slightly from the experiment data at low positron energy. This points to more severe changes in the near-surface region that occur upon prolonged degradation and are not accounted for in the model. This may also affect the fraction of positrons that can diffuse back and annihilate at the surface, changing the surface annihilation fraction $f_s(E)$, which is assumed here to remain the same for all degradation times, identical to that for the as-deposited sample as derived from VEPFIT analysis.

The diffusion coefficient of $D = 35\ \mathrm{nm}^2/\mathrm{h}$ extracted from the analysis should be considered as an apparent diffusion coefficient, since the model assumes that the open volume generated is proportional to the number of in-diffused molecules, while the actual relationship can be more complex. Nevertheless, within this assumption, the apparent diffusion coefficient can be used to estimate the characteristic timescale of in-diffusion of molecules into the ZnO:Al layer with a thickness of $d = 280$ nm. Using $d = 2\sqrt{Dt^*}$, we obtain $t^* = d^2/4D \sim 560$ h, which is the timescale on which the changes in the positron Doppler depth profiling experiments are seen to saturate. Noteworthy, it is remarkably similar to the timescale on which important solar cell parameters such as the series resistance and solar cell efficiency are seen to decay, demonstrating that the process behind the changes in the Doppler depth profiles, i.e., creation of open volume by in-diffusion of molecules, is one of the key processes leading to degradation of the solar cells.

In order to determine the type and concentration of the open volume defects involved, we analyzed the S and W parameters of the ZnO:Al films by comparison to two hydrothermally grown ZnO single crystals, and performed coincidence Doppler broadening (CDB) and positron annihilation lifetime spectroscopy (PALS) experiments described in the next sections, Secs. III D and III E.

D. Doppler broadening identification of the vacancies generated in the ZnO:Al layer

1. Evolution of the S-W points of the top and bottom ZnO:Al layer with degradation time

In order to examine which types of open volume defects correspond to the observed changes in Doppler parameters with degradation time, the S-W points obtained from the conventional layer-model VEPFIT analysis (Sec. III B) for the ZnO:Al top and bottom layer, respectively, are presented in the S-W diagram of Fig. 7.

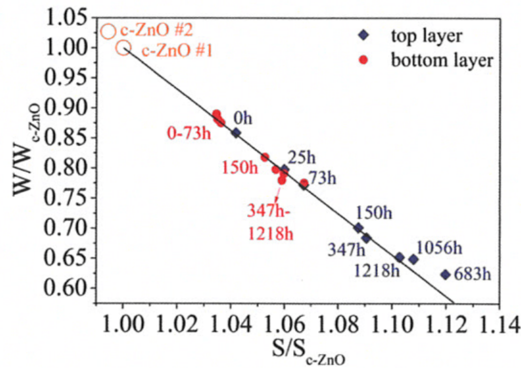

FIG. 7. Evolution of the S-W parameters for the top layer (blue solid diamonds) and bottom layer (red solid circles) of the ZnO:Al with degradation time, presented as a ratio to the S-W parameters of the single crystal c-ZnO No. 1. The orange open circles are the reference S-W points for c-ZnO (No. 1 and No. 2). The solid line indicates the characteristic direction of change in S-W from defect-free ZnO to the Zn monovacancy in ZnO [38–40].

The S-W points were normalized with respect to that of the first ZnO single crystal (c-ZnO No. 1) [34]. The S-W point of the second ZnO single crystal (c-ZnO No. 2) shows a small difference compared to the first ZnO single crystal, which does not affect the main conclusions deduced from the S-W analysis. The solid line indicates the direction of change in S-W parameters going from positron annihilation in defect-free c-ZnO to the characteristic S-W point for positron annihilation in the Zn monovacancy in ZnO [$S(V_{Zn})/S_{ZnO} \cong 1.055$, $W(V_{Zn})/W_{ZnO} \cong 0.81$], where the average of the values reported in [38] and [39] was used. In the interpretation of the (normalized) S-W diagram it should be taken into account that our positron annihilation lifetime and Doppler broadening studies indicated that the HT-grown ZnO crystals contain a significant concentration of positron trapping point defects [34,41–44]. As reported in previous studies on HT-grown c-ZnO, these might correspond to negatively charged substitutional Li on Zn positions (Li_{Zn}^{-}) [45,46] and/or zinc monovacancies decorated with a hydrogen atom ($V_{Zn}:H$) [47,48]. Saturation trapping at such types of defects is expected to lead to a shift in S parameter on the order of $+1\%$ to $+2\%$ for the c-ZnO crystals compared to defect-free ZnO [45–48]. Therefore, the "true" reference point for defect-free ZnO is expected to be located somewhat further away into the top-left direction of Fig. 7, and the S parameter for saturation trapping in Zn monovacancies is expectedly to be located roughly around $S(V_{Zn})/S_{c-ZnO} \sim 1.03$–$1.04$ in this S-W diagram. Also, it should be noted that even normalized values of S and W are affected by the energy resolution of the HPGe detector and the energy windows for S and W [49]. The detector resolution and energy windows employed in this study are close to the corresponding settings of Refs. [38] and [45], resulting in a systematic difference in normalized S of at most -0.3%.

Nevertheless, it is clear that the S-W points for the top and bottom layers of the as-deposited sample are positioned on a line that is very close to the shift direction between the S-W points of ZnO and the Zn monovacancy in ZnO. This indicates that most positrons trap and annihilate in Zn monovacancies in the ZnO:Al film, while some positrons may even annihilate in larger vacancy clusters already for the as-deposited films. Upon degradation, a strong shift towards higher S and lower W is observed, resulting from increased positron trapping in open volume defects with a size larger than a monovacancy [40], consistent with our quantitative results obtained using positron annihilation lifetime spectroscopy (PALS) as described in Sec. III E. The top layer contains more or larger positron trapping vacancy clusters [40] both in the as-deposited state and after prolonged degradation as compared to the bottom ZnO layer, as will be quantitatively discussed in Sec. III E based on our PALS results. Clearly, the quantitatively different behavior in the bottom layer, with less open volume generated compared to the top layer, is consistent with the diffusion model presented in the previous section, Sec. III C.

2. Coincidence Doppler broadening ratio curves

Further support for the presence of these types of vacancy-related defects in the ZnO:Al layer and their evolution upon degradation comes from coincidence Doppler broadening (CDB) spectra collected at a positron implantation energy of 1.4 keV and 5 keV. These energies correspond to mean positron implantation depths centered in the top and the bottom layer of the ZnO:Al TCO, respectively. Figure 8 shows the 1D electron-positron momentum distributions extracted from the CBD measurements, presented as the ratio to the momentum distribution for the ZnO single crystal No. 1.

The ratio curves presented in Fig. 8(a) for the ZnO:Al top layer in the as-deposited state and after 25 h of degradation show very similar features to those for the Zn monovacancy in ZnO reported in previous experimental and theoretical studies [40], indicating the presence of Zn monovacancies already in the as-deposited films. Upon prolonged degradation for 150 to 683 hours, the shape of the ratio curves changes remarkably. The shoulder at 1.3 a.u. and valley around 2 a.u. characteristic for annihilation in Zn monovacancies flatten out. Simultaneously, the intensity at high momenta reduces substantially, while the intensity at low momenta below 0.5 a.u. is seen to increase further. This clearly indicates that positron annihilation at (larger) vacancy clusters starts to dominate after prolonged degradation on a timescale of 150–683 h, consistent with the evolution of the Doppler S and W parameters discussed in Sec. III D 1 and the PALS spectra in Sec. III E.

The features of the ratio curve for the ZnO:Al bottom layer in the as-deposited state presented in Fig. 8(b) are also very similar to the ratio curve calculated for the Zn monovacancy. However, the features are somewhat flattened out towards the bulk reference. Thus, Zn monovacancies are clearly also present in the bottom layer, albeit that the concentration of open volume defects seems smaller than in the top layer. Upon degradation, the ratio curve of the bottom layer increases below 0.5 a.u. and decreases in the full range beyond 0.5 a.u., quite similarly to the ratio curves of the top layer. Nevertheless, the shoulder at 1.3 a.u. and the valley at 2 a.u. remain here distinctly visible, revealing that Zn monovacancies stay more dominant, even though larger vacancy clusters start to contribute for degradation times of 150 h and longer. This

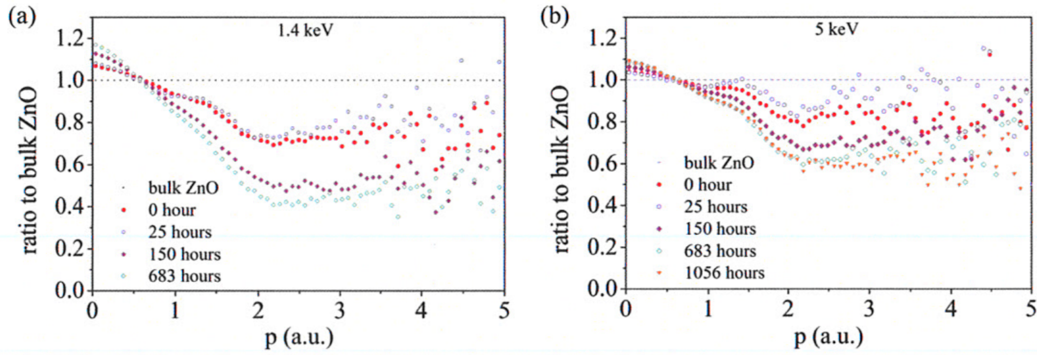

FIG. 8. Ratio curves of the 1D electron-positron momentum distributions as a function of the degradation time, obtained from coincidence Doppler broadening (CDB) measurements at a positron implantation energy of (a) 1.4 keV and (b) 5 keV. The data are presented as the ratio to the 1D electron-positron momentum distribution of c-ZnO No. 1 collected at 12 keV (a.u. = atomic units; 1 a.u. = $7.2974 \times 10^{-3} m_0 c$).

is fully consistent with the evolution of the *S*-*W* point of the bottom layer and the inferred formation of (smaller) vacancy clusters with prolonged degradation, as discussed above in Sec. III D 1, and consistent with the PALS results discussed next in Sec. III E.

E. Evolution of the size of vacancies and vacancy clusters as extracted from positron annihilation lifetime studies

Positron annihilation lifetime spectroscopy (PALS) is a sensitive method to probe the size and concentration of vacancy-related defects. Therefore, positron lifetime spectra were collected at selected positron implantation energies for the ZnO:Al-based CIGS solar cells at various stages of degradation, including 0 h, 73 h, 600 h, 1056 h, and 1218 h of accelerated degradation. The positron lifetime spectra were fitted by using the LT program with four lifetime components. Figure 9 shows the lifetimes and intensity of the two major (short) lifetime components in the spectra for the top layer (corresponding to averaged values obtained from the two PALS spectra collected at 1 and 2 keV) and the bottom layer (collected at 5 keV) of ZnO:Al at the beginning of the degradation process (0 hours and 73 hours) and after long-time degradation (600 hours, 1056 hours, and 1218 hours). The third and fourth positron lifetimes are in the range of 1 to 5 ns, but show very low intensities between 0.2% and 3%, demonstrating that large voids and the corresponding formation of orthopositronium are nearly absent. For the top layer, a short lifetime τ_1 for the as-deposited sample of 224 ± 5 ps is obtained from the LT analysis, which is in the range of 220–240 ps reported for the Zn monovacancy [45,50]. The second lifetime τ_2 of 369 ± 9 ps is due to larger vacancy clusters [Fig. 9(a)], and corresponds to a size on the order of a six-vacancy, since the lifetime is similar to that of a $3V_{Zn}-3V_O$ vacancy cluster according to theoretical calculations presented in [17]. Upon prolonged degradation for $t = 1218$ h, τ_1 and τ_2 of the top layer increase to 256 ± 5 ps and 438 ± 7 ps, respectively, revealing an increase in the size of vacancies. In particular, these lifetimes indicate that multivacancies (possibly trivacancies or four-vacancies such as $V_{Zn}-mV_O$, $m = 2, 3$) [40] and larger vacancy clusters with a typical size similar to 6 missing $V_{Zn}-V_O$ pairs, respectively, are formed in the top layer of ZnO:Al. In the bottom layer of ZnO:Al, the trend is similar to the top layer. However, τ_1 stays more constant in the range of 224 ps to 242 ps during the accelerated degradation process, while the second lifetime τ_2 of 321 ± 8 ps at the beginning of the degradation process is smaller than that in the top layer (369 ± 9 ps), and increases to a value of ~410 ps after prolonged degradation, indicating that the open volume defects in the bottom layer grow also,

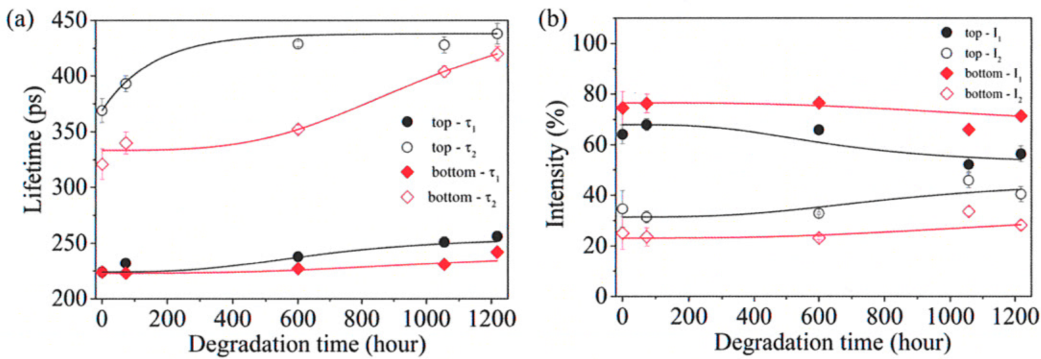

FIG. 9. (a) Positron lifetime τ_1 and τ_2, and (b) intensity I_1 and I_2 for the top and bottom layer of the ZnO:Al TCO of a CIGS solar cell as a function of time of accelerated degradation. Full lines are guides to the eye.

but they stay smaller than in the top layer. Most likely the lifetime of 242 ± 5 ps still corresponds mainly to annihilation in Zn monovacancies with some divacancies present, while the longer lifetime of $\sim$410 ps points to vacancy clusters with a size on the order of 4 missing $V_{Zn}-V_O$ pairs.

As shown in Fig. 9(b), the intensity of the short-lifetime τ_1 component of 64% for the top layer of as-deposited ZnO:Al is about 1.8 times larger than that for the long-lifetime τ_2 component (35%) at the beginning of the degradation process, showing that around two-thirds of positrons trap and annihilate in Zn monovacancies, while around one-third of positrons annihilate in the larger open spaces such as six-vacancies. Upon prolonged degradation, the intensity of the short-lifetime component first remains rather constant up to a degradation time of 600 h, and decreases from 64% to 56% for the longest degradation times, while the fraction for the second lifetime component increases from 35% to 40%. This might indicate that the concentration of large vacancy cluster has increased, leading to increased trapping and annihilation of more positrons in the larger vacancy clusters. However, since the vacancy clusters have grown, it should be noted that the trapping efficiency of the open volume defects may also have increased, which will lead to an increase in the intensity of the second lifetime component as well. For the bottom layer of as-deposited ZnO:Al, 74.5% of positrons trap and annihilate in the Zn monovacancies, while 25% annihilate in the large vacancy clusters at the start of the degradation process. Upon prolonged degradation beyond 600 h, the intensity of the short-lifetime component decreases for the bottom layer also, while the intensity of the second lifetime component increases [Fig. 9(b)], indicating preferred trapping in more abundant larger vacancy clusters for the bottom layer of the ZnO:Al as well. Thus, the bottom layer shows a similar behavior to the top layer, albeit that smaller open space is present and created. The smaller intensity of the second lifetime component compared to that for the top layer indicates that this also leads to less trapping at the vacancy clusters.

Clearly, the shortest lifetime τ_1 corresponds to positron trapping in the Zn monovacancies, which could be located either in the bulk of a ZnO:Al grain or at the grain boundaries of ZnO:Al. Noteworthy, in n-type Al-doped ZnO the formation of Zn monovacancies is favorable [51], where they form the dominant charge compensating acceptor defects [22,52]. Trapping in Zn monovacancies, formed inside ZnO:Al grains during deposition, can thus be expected. However, it should be noted that some of the detected Zn monovacancies could correspond to similarly sized open space at the grain boundaries, since the formation energy of Zn vacancies at grain boundaries is also relatively low compared to the case of pure ZnO [53]. The second lifetime component points to the presence of larger vacancy clusters which most likely are located at the grain boundaries, as was also proposed in some previous studies [50,54] and is inferred from the diffusion model analysis presented above in Sec. III C. The picture thus emerges that the as-deposited ZnO:Al layers contain Zn monovacancies inside the grains and larger vacancy clusters at their grain boundaries. During accelerated degradation, the larger vacancy clusters at the grain boundaries show a pronounced increase in size, while their concentrations possibly do not change significantly except for the longest degradation times of $\sim$1000 h and beyond, as indicated by the positron lifetime intensities.

In the next section we provide evidence for the emerging picture of positron trapping in Zn monovacancies inside the ZnO:Al grains and in larger vacancy clusters at their grain boundaries. The evidence is obtained by analysis of the collected positron annihilation lifetimes and intensities in the framework of a detailed positron trapping model involving grain boundaries and vacancies inside the grains as trapping sites, as developed by Würschum *et al.* [55].

F. Positron trapping model with intragranular vacancies and grain boundary trapping

In the grain boundary positron trapping model presented by Würschum *et al.* [55], the positron annihilation lifetime spectrum is decomposed into components related to the fractions of positrons that trap and annihilate in vacancy-type point defects inside spherically shaped grains and in open-volume-type defects at the grain boundaries, respectively, and further into components associated with bulk "free" positron annihilation in the grains. The positron annihilation lifetime spectra can be written as a sum of exponential decay functions, each characterized by an intensity I_i and lifetime τ_i [55]:

$$n(t) = I_v \exp(-t/\tau_v) + I_b \exp(-t/\tau_b) + \sum_{j=1}^{\infty} I_{0,j} \exp(-\lambda_{0,j} t), \quad (13)$$

where I_v and τ_v are the annihilation fraction and positron lifetime in the vacancy-type defects inside the grain, I_b and τ_b are the corresponding positron annihilation parameters associated with the open-volume-type defects in the grain boundaries, and further a sequence of decay rates $\lambda_{0,j}$ with associated annihilation fractions $I_{0,j}$, corresponding to a modification of the conventional bulk "free" positron annihilation induced by the diffusion-limited positron trapping in vacancies and at grain boundaries.

We employed the positron trapping model to simulate the positron annihilation fractions in vacancies inside the grain and in the grain boundaries. In this model [34], 7 empirical parameters are required, namely r_0 the radius of the grains, D_+ and τ_f, the positron diffusion coefficient and positron lifetime in the bulk of the grain, respectively, σ_v and τ_v, the positron trapping coefficient and positron lifetime of vacancies inside the grain, and finally α and τ_b, the trapping rate at the grain boundaries and positron lifetime of the open-volume defects at the grain boundaries, respectively. The parameters deduced for the studied ZnO layers are listed in Table III. Among these parameters, a grain radius $r_0 = 62 \pm 2$ nm for the ZnO:Al layer in the as-deposited CIGS sample and $r_0 = 58 \pm 2$ nm after degradation for 1056 h, indicating that the grain size had not changed, was derived from cross-sectional SEM measurements [34]. A positron lifetime of $\tau_{V_{Zn}} = 224 \pm 5$ ps for the monovacancy V_{Zn} inside the grains and a positron lifetime of $\tau_b = 369 \pm 9$ ps (top layer) and of $\tau_b = 321 \pm 8$ ps (bottom layer)

TABLE III. Parameters used in the positron trapping model [34,55].

ZnO:Al	Parameter name	Symbols	Parameter value: As-deposited	Parameter value: 1056-hour degradation
Grain	Positron lifetime V_{Zn}	$\tau_{V_{Zn}}$	224 ps	251 ps (top) 231 ps (bottom)
	Trapping coefficient V_{Zn}	$\sigma_{V_{Zn}}$	1.7×10^3 ps^{-1} [a,b]	1.7×10^3 ps^{-1} [a,b]
	Positron diffusion coefficient	D_+	520 nm^{2}ps^{-1} [b]	520 nm^{2}ps^{-1} [b]
	Free positron lifetime	τ_f	161 ps [c]	161 ps [c]
Grain boundary	Grain radius	r_0	62 nm	58 nm
	Trapping rate at the grain boundary	α	1.5 nmps^{-1} (top) 1 nmps^{-1} (bottom) [d]	1.5 nmps^{-1} (top) 1 nmps^{-1} (bottom) [d]
	Positron lifetime grain boundary	τ_b	369 ps (top) 321 ps (bottom)	428 ps (top) 404 ps (bottom)

[a]Reference [16].
[b]Reference [47].
[c]Reference [56].
[d]Reference [57].

for the vacancy clusters at grain boundaries were obtained from the PALS spectra reported in the previous section. After degradation, the experimentally extracted positron lifetimes increase significantly. Therefore, in the simulations performed for the comparison with the 1056-h degraded sample, the corresponding experimental lifetimes were included (see Table III).

Figure 10(a) presents the average lifetime in the top and bottom layers of the ZnO in the as-deposited CIGS samples calculated using this model as a function of C_v, the concentration of the vacancy-type defects inside the grain. For small vacancy concentrations ($\sim 10^{-6}$), most positrons diffuse to the grain boundaries and are trapped there, while a fraction of $\sim 5\%$ also annihilates as bulk "free" positrons inside the grains. With an increase of C_v, positrons increasingly trap

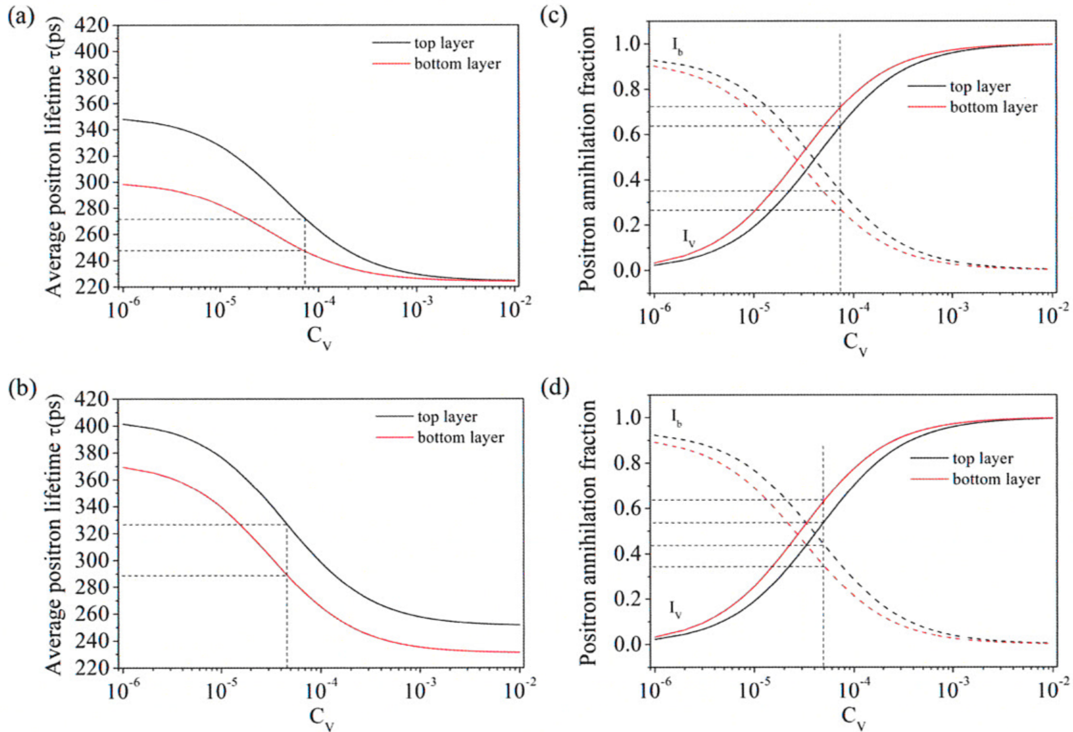

FIG. 10. Left: Average positron lifetime as a function of vacancy concentration C_v inside the grains for (a) as-deposited ZnO:Al and (b) 1056-h degraded ZnO:Al films, calculated using the positron trapping model of [55] using the parameters given in Table III. Dashed horizontal lines correspond to the measured PALS results. Right: Calculated positron annihilation fractions in vacancies inside the grains and at the grain boundaries as a function of vacancy concentration for (c) as-deposited ZnO:Al and (d) 1056-h degraded ZnO:Al films.

and annihilate at point defects in the grain, leading to a reduction in the average positron lifetime. At large values of C_v, this process becomes dominant and the average lifetime $\bar{\tau}$ approaches $\tau_{V_{Zn}}$.

The experimentally observed average positron lifetime of 247 ± 3 ps for the bottom layer can be used to derive the corresponding concentration of intragranular point defects V_{Zn} of $C_V = 7 \times 10^{-5}$, as indicated by the dashed lines in Fig. 10(a). It is reasonable to assume that the concentration of vacancies for the top layer is about the same as for the bottom layer. Within the positron trapping model, consistency with the observed positron annihilation parameters, including the average positron lifetime of 271 ± 3 ps for the top layer, is maintained, requiring only a slight increase in the trapping rate of positrons at the grain boundaries of $\alpha = 1.5$ nmps^{-1} in the top layer. Such a higher trapping rate can be understood, since the size of the open volume defects at the grain boundaries is clearly larger in the top layer compared to the bottom layer, and therefore they can act as stronger positron trapping sites.

Also, the positron annihilation fractions are consistently retrieved using the positron trapping model with parameters given in Table III. Figure 10(c) shows the calculated positron annihilation fractions in vacancies inside the grains (I_v) and at the grain boundaries (I_b) upon variation of intragranular vacancy concentration C_V for the ZnO:Al film in the as-deposited CIGS samples. Clearly, with increasing intragranular vacancy concentration C_V, the annihilation fraction in the monovacancies I_v increases while I_b decreases for both the top and bottom layers of the ZnO:Al layer. Using the extracted concentration of $C_V = 7 \times 10^{-5}$ [Fig. 10(a)], the calculated fractions I_v and I_b are 63% and 35% for the top layer, respectively, while for the bottom layer calculated fractions of I_v and I_b of respectively 71% and 28% are obtained. These positron annihilation fractions in vacancies inside the grains and at the grain boundaries are in a good quantitative agreement with the intensities determined from the experimental PALS spectra of $I_v = 64\%$ and $I_b = 35\%$, respectively, for the top layer, and $I_v = 74.5\%$ and $I_b = 25\%$, respectively, for the bottom layer of the as-deposited sample. Notably, the model accurately reproduces the larger annihilation fraction at the grain boundaries for the top layer compared to the bottom layer, showing the consistency of the applied positron trapping model.

A similar analysis was performed for the Al-doped ZnO layer for the 1056-h degraded sample. Figures 10(b) and 10(d) present the corresponding average lifetime and positron annihilation fractions for the top layer and bottom layer as a function of intragranular vacancy concentration C_V. In the positron trapping model, only the (experimentally determined) values for the positron lifetimes of the vacancies in the grain and of the vacancy clusters at the grain boundaries were changed as input parameters in the calculations (see Table III), which turned out to be sufficient to retrieve consistency with all experimental results from the positron lifetime study.

Figure 10(b) shows that an intragranular vacancy concentration of about $C_V = 5 \times 10^{-5}$ for both the top and bottom layers of ZnO:Al is now deduced, using the average lifetime $\bar{\tau} = 327 \pm 3$ ps for the top layer and $\bar{\tau} = 288 \pm 3$ ps for the bottom layer as obtained from the PALS spectra, indicating that the concentration of vacancies inside the grains remains nearly constant. Figure 10(d) presents calculated fractions of I_v and I_b, inferring annihilation fractions of $I_v = 52\%$ and $I_b = 45\%$, respectively, for top layer and $I_v = 61\%$ and $I_b = 37\%$, respectively, for bottom layer using $C_V = 5 \times 10^{-5}$. This shows that the fraction of positrons that trap and annihilate at vacancies inside the grains (I_v) decreases, while annihilation at the grain boundaries (I_b) increases, consistent with the observed experimental trends given in Fig. 9(b) for prolonged degradation of ~1000 h and more.

In conclusion, the positron trapping model consistently shows that most positrons (60%–70%) trap and annihilate in Zn monovacancies V_{Zn} inside the grains, while 30%–40% of positrons trap and annihilate in vacancy clusters $(V_{Zn})_m(V_O)_n$ at the grain boundaries, with a higher fraction of positrons annihilating in larger vacancy clusters in the top layer compared to the bottom layer. The model also demonstrates that the fraction of positrons annihilating from a bulklike "free" delocalized state is small for all studied samples, consistent with the absence of a short bulklike lifetime component in the positron annihilation lifetime spectra.

G. Degradation mechanism

An important factor in the decrease in efficiency of the CIGS solar cell is the deterioration of the ZnO:Al transparent conductive oxide window layer. In this study, a strong increase and corresponding decrease in respectively the *S* and *W* parameter of the ZnO:Al layer is observed in the positron annihilation depth profiling experiments, that evolve on a remarkably similar timescale as the decrease in solar cell efficiency. This marks the development of increased open volume defect densities and sizes of the vacancy clusters at the grain boundaries, and possibly also inside the grains, that bears a direct relationship to the degradation of the CIGS solar cells. In contrast, no visible change in *S* or *W* parameter of the CIGS layer emerged from the depth-resolved experiments.

In previous studies, the degradation of the ZnO:Al TCO was linked to the formation of $Zn(OH)_2$ and Zn-based carbonates including mixtures of these, i.e., $Zn_x(OH)_y(CO_3)_z$, at the grain boundaries due to the reaction with ZnO of H_2O and CO_2 molecules after diffusion into the layer via the grain boundaries. The present study indicates that the creation of open volume in the ZnO:Al layer also plays an essential role in the degradation. A substantial fraction of positrons is observed to trap and annihilate at the grain boundaries in the ZnO:Al film with grain sizes of ~60 nm. Clearly, a strong increase in the size of the open volume at the grain boundaries is revealed. In addition, part of the positrons trap in V_{Zn} monovacancies or in small V_{Zn} vacancy complexes, and a minor increase in their size with degradation is also observed. Two related processes could thus possibly be involved in the degradation of the ZnO:Al layer treated in the damp-heat chamber (85 °C/85% RH).

The first, most important process is related to the grain boundaries of the Al-doped ZnO layer. At the grain boundary, not-fully-passivated zinc, oxygen, and aluminum ions will be present. Under the condition of 85 °C/85% RH, small molecules like H_2O and carbon dioxide from the environment diffuse into the grain boundary and contribute to the formation of $Zn(OH)_2$ complexes and Zn-based carbonates from reaction of the ZnO:Al with the water and CO_2 molecules [8].

This means that Zn and O atoms will be locally removed from the ZnO lattice, and vacancies and small vacancy clusters can be formed at the grain boundaries.

Clearly, the timescale of diffusion extracted from the formation concentration profile of vacancies and vacancy clusters, on the order of $t^* = \frac{d^2}{4D} \sim 560$ h, is similar to that of the in-diffusion of environmental molecules, extracted from SIMS profiles in previous studies by Theelen [58] and by Hüpkes [59]. Indeed, the diffusion coefficient of $D = 35\ \mathrm{nm}^2/\mathrm{h}$ extracted from the positron depth-profiling studies is of the same order of magnitude as the one extracted from SIMS profiles of in-diffused deuterium, $D_{D^+} \sim 100\ \mathrm{nm}^2/\mathrm{h}$ [59], which arguably is related to in-diffusion via the grain boundaries. Thus, the present study provides further support for the conclusion that in-diffusion of molecular species via grain boundaries is a major cause for degradation of the ZnO:Al layer. A similar mechanism was also reported for polycrystalline H-doped In_2O_3 (IO:H) [60]. Here, pronounced formation of open volume defects at the grain boundaries is observed, directly connected to the occurrence of chemical reactions and formation of $Zn(OH)_2$, Zn-based carbonates, and mixtures of these [e.g., $Zn_x(OH)_y(CO_3)_z$] inferred from previous studies. The formed Zn-based compounds together with the increase in open space at the grain boundaries will effectively disturb lateral charge carrier transport through the ZnO:Al TCO layer, by imposing increasingly large transport barriers and reducing charge carrier mobility due to enhanced scattering at the grain boundaries. Moreover, charge carriers could be more effectively trapped and/or suffer from nonradiative recombination at the open space formed at grain boundaries, reducing the charge carrier density. These factors will lead to a strong increase in series resistance (as observed), and correspondingly, a large reduction in fill factor and efficiency of the ZnO:Al/i-ZnO/CdS/CIGS/Mo solar cells. In actual modules, ZnO:Al TCO layers with a larger thickness of typically $\sim 1\ \mu$m are used, leading to substantially slower, but otherwise similar, degradation of the solar cell fill factor.

A second, minor degradation process might occur inside the grains, related to formation of divacancies out of Zn monovacancies present inside the grains of the as-deposited ZnO:Al. Namely, it was observed in [8] and [59] that H^+ is formed in the films during damp-heat treatment for prolonged degradation times. Especially, H^+ showed high concentrations in the top 100 nm of ZnO:Al films [8]. The formed H^+ may easily enter the grain, where fast in-diffusion via interstitial sites is expected, in view of the very high diffusion coefficient in ZnO of $D_{\mathrm{H}_i} \sim 10^7 \mathrm{nm}^2/\mathrm{h}$ (at 380 K) [61,62]. H^+ may occupy body-centered interstitial sites in ZnO, where it leads to plastic deformation of the ZnO crystal lattice, and the formation of additional Zn monovacancies and growth of larger vacancies such as $V_{\mathrm{Zn}}-V_{\mathrm{O}}$ inside the grain can therefore be expected [63,64]. Indeed, in the positron lifetime experiment, the corresponding shortest lifetime τ_1 of the top ZnO:Al increases to 256 ± 5 ps during prolonged degradation, indicating that larger vacancies are created. These point defects may also contribute to increased scattering of charge carriers and the observed increase in series resistance of the CIGS solar cell. Nevertheless, this study shows that the in-diffusion of molecules via grain boundaries and the formation of open volume at the grain boundaries form the key (and rate-limiting) factor to the degradation of the ZnO:Al. This is underlined by the observed diffusion coefficient of $D = 35\ \mathrm{nm}^2/\mathrm{h}$, demonstrating that this rate-limiting step is orders of magnitude slower than interstitial diffusion of H^+ with a diffusion coefficient of $D_{\mathrm{H}_i} \sim 10^7 \mathrm{nm}^2/\mathrm{h}$, while larger species such as O_2, H_2, H_2O, and CO_2 will show negligible diffusion into the ZnO grains [65].

IV. CONCLUSIONS

The accelerated degradation of Al-doped ZnO TCO layers on top of CIGS solar cells was examined using various positron annihilation techniques. The PALS and Doppler broadening studies indicate that the formation and growth of vacancy clusters at grain boundaries is a key component of the degradation mechanism of the ZnO:Al/i-ZnO/CdS/CIGS/Mo solar cells. Quantitative information on the sizes of the vacancy clusters and fractions of positrons trapping at the grain boundaries was obtained by detailed comparison of the positron annihilation lifetime results to a positron trapping model developed by Würschum *et al.* [55]. The evolution of open volume at the grain boundaries may contribute substantially to increase transport barriers upon degradation, reducing charge carrier mobility, and may further give rise to increased charge carrier trapping. The formation and growth of open volume at the grain boundaries in the ZnO:Al TCO layer thus forms a major factor to the observed large increase in series resistance and the reduction in solar cell fill factor, which is the main cause for the largely reduced solar cell efficiency upon prolonged moisture-heat degradation for solar cells without a costly water-protective glass-based packaging.

Positron Doppler depth profiling is shown to be a sensitive method to monitor the depth-resolved vacancy generation as a function of degradation time. The positron study establishes a direct correlation between the depth profiles of the generated vacancy clusters and the previously observed in-diffusion of molecules such as H_2O and CO_2 via the grain boundaries of the ZnO:Al TCO layer, with a convincing match in the characteristic timescale of diffusion and solar cell degradation, providing further evidence for a key role in the degradation. This infers that the reactions of these molecules at the grain boundaries lead to the creation of the observed additional open volume. The formation of H^+ at the grain boundaries might also affect the degradation via a second process, in which H^+ enters and rapidly diffuses into the ZnO:Al grains, where the H^+ ions may cause plastic deformation of the ZnO lattice leading to an increase in size of Zn vacancies. The mechanisms of degradation suggest that synthesis methods should be explored which either lead to a reduced density of grain boundaries or the use an additional suitable barrier layer to prevent infiltration of environmental molecules.

ACKNOWLEDGMENTS

We thank Martijn de Boer for technical assistance in the positron annihilation studies. The research by W.S. at Delft University of Technology was supported by a China Scholarship Council (CSC) grant. We acknowledge financial support for this research from ADEM, A green Deal in Energy Materials of the Ministry of Economic Affairs of The Nether-

lands [66]. The POSH facility at the Reactor Institute Delft (RID) was used for the CDB measurements. The PALS study is based on experiments performed at the PLEPS instrument of the NEPOMUC facility at the Heinz Maier-Leibnitz Zentrum (MLZ), Garching, Germany, and was supported by the European Commission under the 7th Framework Programme, Key Action: Strengthening the European Research Area, Research Infrastructures, Contract No. 226507, NMI3.

APPENDIX: DIFFUSION-INDUCED CHANGES IN POSITRON DOPPLER BROADENING DEPTH PROFILES

In this Appendix a model is described in order to account for the effect of a diffusion-related depth distribution on positron Doppler broadening depth profiles. To the authors' knowledge, a similar model has not been reported in the literature. The diffusion model assumes that the formation of additional open volume is proportional to the concentration of in-diffused molecules, and in turn the created open volume defects lead to a proportional increase of ΔS and decrease of ΔW. The starting point is the solution for diffusion in a semi-infinite homogeneous medium with a constant diffusion coefficient D, taking as the boundary condition a constant concentration $C(0)$ at the surface, given by [35]

$$C(z) = C(0)\mathrm{erfc}\left(\frac{z}{2\sqrt{Dt}}\right), \tag{A1}$$

where $C(z)$ is the concentration as a function of depth z below the surface, $\mathrm{erfc}(x) = 1 - \mathrm{erf}(x)$ is the complementary error function, and t is the degradation time. In order to derive the dependence on positron implantation energy of $\Delta S(E)$ and $\Delta W(E)$, Makhovian distributions for the positron implantation profiles were used, given by

$$P(z,E) = \frac{2}{z_0}\left(\frac{z}{z_0}\right)^{m-1} e^{-(z/z_0)^m}, \tag{A2}$$

where $z_0 = 1.13 z_{\mathrm{ave}}$ with the average positron implantation depth $z_{\mathrm{ave}} = \alpha_p E^n/\rho$, ρ is the density of the medium, and E is the positron implantation energy. In the analysis, the parameters $m = 2$, $n = 1.62$, and $\alpha_p = 4.0 \mu\mathrm{g\,cm^{-2}\,keV^{-1.62}}$ were used [28,36].

The depth dependence of the concentration of in-diffusion atmospheric species in the diffusion model and the positron stopping profile given by Eqs. (A1) and (A2) can be used to derive expressions for the change in S and W parameters as a function of positron implantation energy. If one assumes that the open volume generated is proportional to the concentration of in-diffused atomic and molecular species and leads to a proportional change in S and W, the change in S parameter, $\Delta S(E)$, and in W parameter, $\Delta W(E)$, at a specific positron implantation energy is given by the integrated product of the concentration depth profile and the Makhovian implantation profile for positron implantation energy E,

$$\Delta S(E,t) = I_{\Delta S}\int_0^\infty C(z)P(z,E)dz, \tag{A3}$$

$$\Delta W(E,t) = I_{\Delta W}\int_0^\infty C(z)P(z,E)dz, \tag{A4}$$

where $I_{\Delta S}$ and $I_{\Delta W}$ are proportionality prefactors. Diffusion of thermalized positrons is not taken into account in the model. This limits the validity of the model to the case where the positron diffusion length $L_+ \ll z_0$ [28,37], i.e., for films with moderate to high defect concentrations leading to a short positron diffusion length, or to sufficiently high positron implantation energies.

Using the expressions for the concentration depth profile Eq. (A1) and the Makhovian implantation profile Eq. (A2), the integral in Eqs. (A3) and (A4) can be rewritten as follows:

$$\begin{aligned}
&\int_0^\infty \mathrm{erfc}\left(\frac{z}{2\sqrt{Dt}}\right)\frac{2z}{z_0^2}e^{-(z/z_0)^2}dz \\
&= \int_0^\infty \left[1-\mathrm{erf}\left(\frac{z}{2\sqrt{Dt}}\right)\right]\frac{2z}{z_0^2}e^{-(z/z_0)^2}dz \\
&= \int_0^\infty \frac{2z}{z_0^2}e^{-(z/z_0)^2}dz - \int_0^\infty \mathrm{erf}\left(\frac{z}{2\sqrt{Dt}}\right)\frac{2z}{z_0^2}e^{-(z/z_0)^2}dz \\
&= 1 - \frac{z_0}{\sqrt{z_0^2+4Dt}},
\end{aligned} \tag{A5}$$

where we used the table of integrals reported by Ng and Geller in Ref. [67] to solve for the second integral.

This means that the positron-implantation energy dependent change in S and W can be described by

$$\Delta S(E) = \Delta S_0\left[1 - \frac{z_0}{\sqrt{z_0^2+4Dt}}\right],$$

$$\Delta W(E) = \Delta W_0\left[1 - \frac{z_0}{\sqrt{z_0^2+4Dt}}\right], \tag{A6}$$

valid for one-dimensional diffusion in a semi-infinite medium. This is also a good approximation for the case of a finite layer with thickness d, provided that the diffusion length $L = \sqrt{Dt} \ll d$, or, for the case $L = \sqrt{Dt} \sim d$, that the average positron implantation depth $z_{\mathrm{ave}} = 1.13 z_0 \ll d$, i.e., for low positron implantation energies. For the case of $L = \sqrt{Dt} \sim d$ or larger (i.e., for long degradation times), the solution of the diffusion problem of a finite slab instead of a semi-infinite planar medium for the concentration profile $C(z)$ needs to be considered [35]. Here, we neglect the corresponding (moderate) changes in the concentration profile $C(z)$ that first primarily occur near the ZnO/CdS interface, since these expectedly will have a minor effect on the Doppler depth profiles in this study, in view of the broad positron implantation profiles at the high positron energies required to probe the region of the ZnO/CdS interface ($z_0 \sim d$). In the equations, $\Delta S_0 = I_{\Delta S}C(0)$ and $\Delta W_0 = I_{\Delta W}C(0)$ are the change in S and W for annihilation of thermalized positrons inside the ZnO:Al just below the surface, with $I_{\Delta S}$ and $I_{\Delta W}$ intensity proportionality prefactors connecting ΔS_0 and ΔW_0 with the surface concentration $C(0)$.

In general, an integral over a finite slab extending to $z_{\mathrm{max}} = d$ instead of an integration over a semi-infinite system needs to be performed, in order to properly include the behavior of $\Delta S(E)$ and $\Delta W(E)$ at high positron implantation energies. The corresponding integral can be solved numerically,

according to

$$\Delta S_{\mathrm{ZnO:Al}}(E) = \Delta S_0\left[1 - e^{-(d/z_0)^2} - \int_0^d \mathrm{erf}\left(\frac{z}{2\sqrt{Dt}}\right)\frac{2z}{z_0^2}e^{-(z/z_0)^2}dz\right] \quad \text{(A7)}$$

and

$$\Delta W_{\mathrm{ZnO:Al}}(E) = \Delta W_0\left[1 - e^{-(d/z_0)^2} - \int_0^d \mathrm{erf}\left(\frac{z}{2\sqrt{Dt}}\right)\frac{2z}{z_0^2}e^{-(z/z_0)^2}dz\right]. \quad \text{(A8)}$$

The cutoff at $z = d$ takes into account that at high positron implantation energies more and more positrons annihilate in the CdS and CIGS layers underneath the ZnO:Al layer [28,37], and do not probe the degradation-induced changes in the ZnO layer. The model assumes that the CdS and CIGS layers are not affected significantly by the in-diffusion of molecules.

In order to provide the connection to the experimentally observed depth profiles, we start by noting that the depth profiles for the as-deposited sample $S_{\mathrm{AD}}(E)$ and $W_{\mathrm{AD}}(E)$ can be written as

$$S_{\mathrm{AD}}(E) = S_s(t=0)f_s(E) + S_{\mathrm{ZnO:Al}}(t=0)f_1(E) + S_2(t=0)f_2(E), \quad \text{(A9)}$$

$$W_{\mathrm{AD}}(E) = W_s(t=0)f_s(E) + W_{\mathrm{ZnO:Al}}(t=0)f_1(E) + W_2(t=0)f_2(E), \quad \text{(A10)}$$

where S_s, $S_{\mathrm{ZnO:Al}}$, and S_2 are the S parameter for the surface, the ZnO:Al layer, and the CdS/CIGS layer, respectively, and $f_s(E)$, $f_{\mathrm{ZnO:Al}}(E)$, and $f_2(E)$ are the positron implantation energy dependent fractions of positrons annihilating at the surface and in the two layers, respectively.

The difference in S and in W parameter, extracted from the experimentally observed depth profiles of the degraded ZnO:Al layer relative to that of the as-deposited solar cell, is defined by

$$\Delta S_{\mathrm{exp}}(E,t) = S_{\mathrm{exp}}(E,t) - S_{\mathrm{AD}}(E), \quad \text{(A11)}$$

$$\Delta W_{\mathrm{exp}}(E,t) = W_{\mathrm{exp}}(E,t) - W_{\mathrm{AD}}(E), \quad \text{(A12)}$$

and is in general caused by both the depth-dependent changes in the ZnO layer and at the surface. The latter is described by degradation-time-dependent surface annihilation parameters $S_s(t)$ and $W_s(t)$. In order to separate both contributions, we assume that the surface annihilation fraction $f_s(E)$ does not change upon degradation; i.e., back diffusion and surface trapping of positrons as well as annihilation of epithermal positrons remain unaffected by the degradation. In that case, one can subtract the factor $\Delta S_s f_s(E)$ and $\Delta W_s f_s(E)$ from Eqs. (A11) and (A12) to retrieve the net change in S and W related to positron annihilation in the ZnO:Al layer.

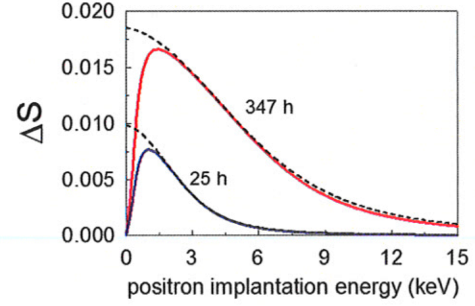

FIG. 11. $\Delta S(E)[1 - f_s(E)]$ curves for 25 h and 347 h of degradation obtained using VEPFIT (full lines, model 1; see text) and $\Delta S(E) = \Delta S_0 \times (1 - z_0/\sqrt{z_0^2 + 4Dt})$ (dashed lines) for a semi-infinite ZnO medium, with $D = 35$ nm^2/h.

Subsequently, the experimental results can finally be compared to the in-diffusion model given by Eqs. (A7) and (A8), according to

$$\Delta S_{\mathrm{ZnO:Al}}(E,t)[1 - f_s(E)] = \Delta S_{\mathrm{exp}}(E,t) - \Delta S_s(t)f_s(E), \quad \text{(A13)}$$

$$\Delta W_{\mathrm{ZnO:Al}}(E,t)[1 - f_s(E)] = \Delta W_{\mathrm{exp}}(E,t) - \Delta W_s(t)f_s(E), \quad \text{(A14)}$$

in which the factor $1 - f_s(E)$ accounts for the reduction in positron annihilation fraction in the ZnO:Al layer in the low-energy range, since upon implantation at shallow depths, surface annihilation becomes a dominant factor. Equations (A13) and (A14) are used to compare the experimental depth profiles with theoretical curves obtained from the diffusion model.

For completeness we demonstrate in Fig. 11 that the diffusion analysis can also be incorporated into VEPFIT. Two simulations of the in-diffusion for degradation times of 25 h and 347 h, respectively, by VEPFIT are shown, using S parameter depth profiles $\Delta S(z) = \Delta S_0[1 - \mathrm{erf}(\frac{z}{2\sqrt{Dt}})]$ as input to the model 1 option of VEPFIT [28], with a diffusion coefficient of $D = 35$ nm^2/h as input parameter. The VEPFIT curves are based on a 22-point discrete $\Delta S_i(z_i)$ depth profile for the ZnO layer and a short positron diffusion length of 2 nm to satisfy the assumption of $L_+ \ll z_0$. In the figure are also the curves obtained from the analytical case of an in-diffusion model with $L_+ \ll z_0$ for a semi-infinite medium, corresponding to $\Delta S(E) = \Delta S_0(1 - \frac{z_0}{\sqrt{z_0^2+4Dt}})$ given in Eq. (A6). For short in-diffusion times, a close agreement is obtained, while for a diffusion time of 347 h, the VEPFIT curve is slightly lower than the curve for this analytical model for a semi-infinite medium at high positron implantation energies, reflecting the finite thickness of the ZnO layer. The agreement supports the reliability of the in-diffusion model analysis based on Eqs. (A7) and (A8). Furthermore, it shows that in principle positron diffusion can also be included as a refinement of the analysis by subsequent VEPFIT analysis for cases where $L_+ \ll z_0$ is not satisfied.

[1] Christian Roselund, PV Magazine, https://www.pv-magazine.com/2016/06/15/zsw-sets-new-thin-film-solar-world-record-with-22-6-efficient-cigs-pv-cell_100024995 (2016).
[2] P. Jackson, D. Hariskos, R. Wuerz, O. Kiowski, A. Bauer, T. M. Friedlmeier, and M. Powalla, Phys. Status Solidi RRL **9**, 28 (2015).
[3] P. Xin, J. K. Larsen, F. Deng, and W. N. Shafarman, Sol. Energy Mater. Sol. Cells **157**, 85 (2016).
[4] D. Jordan and S. Kurtz, in *Proceedings of the 37th IEEE Photovoltaics Specialists Conference (PVSC)* (IEEE, Piscataway, NJ, 2011), p. 827.
[5] J. del Cueto, S. Rummel, B. Kroposki, C. Osterwald, and A. Anderberg, in *Proceedings of the 33rd IEEE Photovoltaics Specialists Conference (PVSC)* (IEEE, Piscataway, NJ, 2008), p. 1.
[6] C. Radue and E. E. van Dyk, Physica B (Amsterdam, Neth.) **404**, 4449 (2009).
[7] M. Theelen and F. Daume, Sol. Energy **133**, 586 (2016).
[8] M. Theelen, T. Boumans, F. Stegeman, F. Colberts, A. Illiberi, J. van Berkum, N. Barreau, Z. Vroon, and M. Zeman, Thin Solid Films **550**, 530 (2014).
[9] D.-K. Kim and H. B. Kim, Curr. Appl. Phys. **13**, 2001 (2013).
[10] M. Hafemeister, S. Siebentritt, J. Albert, M. Ch. Lux-Steiner, and S. Sadewasser, Phys. Rev. Lett. **104**, 196602 (2010).
[11] D. Abou-Ras, B. Schaffer, M. Schaffer, S.S. Schmidt, R. Caballero, and Th. Unold, Phys. Rev. Lett. **108**, 075502 (2012).
[12] A. Chirilă, P. Reinhard, F. Pianezzi, P. Bloesch, A. R. Uhl, C. Fella, L. Kranz, D. Keller, C. Gretener, H. Hagendorfer, D. Jaeger, R. Erni, S. Nishiwaki, S. Buecheler, and A. N. Tiwari, Nat. Mater. **12**, 1107 (2013).
[13] M. Theelen, R. Hendrikx, N. Barreau, H. Steijvers, and A. Böttger, Sol. Energy Mater. Sol. Cells **157**, 943 (2016).
[14] S. W. H. Eijt, H. Leegwater, H. Schut, A. Anastasopol, W. Egger, L. Ravelli, C. Hugenschmidt, and B. Dam, J. Alloys Compd. **509**, S567 (2011).
[15] F. Tuomisto and I. Makkonen, Rev. Mod. Phys. **85**, 1583 (2013).
[16] R. Krause-Rehberg and H. Leipner, *Positron Annihilation in Semiconductors: Defect Studies* (Springer Verlag, Berlin, 1999).
[17] Z. Q. Chen, M. Maekawa, S. Yamamoto, A. Kawasuso, X. L. Yuan, T. Sekiguchi, R. Suzuki, and T. Ohdaira, Phys. Rev. B **69**, 035210 (2004).
[18] D. Scorticati, A. Illiberi, T. C. Bor, S. W. H. Eijt, H. Schut, G. R. B. E. Römer, M. Klein Gunnewiek, A. T. M. Lenferink, B. J. Kniknie, R. Mary Joy, M. S. Dorenkamper, D. F. de Lange, C. Otto, D. Borsa, W. J. Soppe, and A. J. Huis in't Veld, Acta Mater. **98**, 327 (2015).
[19] C. G. Van de Walle, Phys. Rev. Lett. **85**, 1012 (2000).
[20] J. Čížek, J. Valenta, P. Hruška, O. Melikhova, I. Procházka, M. Novotný, and J. Bulíř, Appl. Phys. Lett. **106**, 251902 (2015).
[21] E. H. Kahn, M. H. Weber, and M. D. McCluskey, Phys. Rev. Lett. **111**, 017401 (2013).
[22] F. Tuomisto, V. Ranki, K. Saarinen, and D. C. Look, Phys. Rev. Lett. **91**, 205502 (2003).
[23] G. Brauer, W. Anwand, D. Grambole, J. Grenzer, W. Skorupa, J. Čížek, J. Kuriplach, I. Procházka, C. C. Ling, C. K. So, D. Schulz, and D. Klimm, Phys. Rev. B **79**, 115212 (2009).
[24] F. A. Selim, M. H. Weber, D. Solodovnikov, and K. G. Lynn, Phys. Rev. Lett. **99**, 085502 (2007).
[25] F. Couzinie-Devy, E. Cadel, N. Barreau, L. Arzel, and P. Pareige, Appl. Phys. Lett. **99**, 232108 (2011).
[26] M. Theelen, N. Barreau, F. Daume, H. Steijvers, V. Hans, A. Liakopoulou, Z. Vroon, and M. Zeman, Proc. SPIE **9179**, 91790I (2014).
[27] L. Chai, M.S. dissertation, Delft University of Technology, 2010.
[28] A. van Veen, H. Schut, J. de Vries, R. A. Hakvoort, and M. R. IJpma, AIP Conf. Proc. **218**, 171 (1991).
[29] P. J. Schultz and K. G. Lynn, Rev. Mod. Phys. **60**, 701 (1988).
[30] C. V. Falub, S. W. H. Eijt, P. E. Mijnarends, H. Schut, and A. van Veen, Nucl. Instrum. Methods Phys. Res., Sect. A **488**, 478 (2002).
[31] P. Sperr, W. Egger, W. Kögel, G. Dollinger, C. Hugenschmidt, R. Repper, and C. Piochacz, Appl. Surf. Sci. **255**, 35 (2008).
[32] C. Hugenschmidt, B. Löwe, J. Mayer, C. Piochacz, P. Pikart, R. Repper, M. Stadlbauer, and K. Schreckenbach, Nucl. Instrum. Methods Phys. Res., Sect. A **593**, 616 (2008).
[33] D. Giebel and J. Kansy, Mater. Sci. Forum **666**, 138 (2011).
[34] See Supplemental Material at http://link.aps.org/supplemental/10.1103/PhysRevMaterials.2.105403 for the positron annihilation characterization of the two ZnO single crystals, two alternative models for the *S* parameter depth profiles, the details of the positron trapping model with intragranular vacancies and grain boundary trapping, and SEM analysis of as-deposited and degraded samples.
[35] J. Crank, *The Mathematics of Diffusion*, 2nd ed. (Oxford University Press, Oxford, 1979).
[36] A. Vehanen, K. Saarinen, P. Hautojärvi, and H. Huomo, Phys. Rev. B **35**, 4606 (1987).
[37] A. Zubiaga, J. A. García, F. Plazaola, F. Tuomisto, J. Zúñiga-Pérez, and V. Muñoz-Sanjosé, Phys. Rev. B **75**, 205305 (2007).
[38] A. Zubiaga, F. Tuomisto, V. A. Coleman, H. H. Tan, C. Jagadish, K. Koike, S. Sasa, M. Inoue, and M. Yano, Phys. Rev. B **78**, 035125 (2008).
[39] M. H. Weber, F. A. Selim, D. Solodovnikov, and K. G. Lynn, Appl. Surf. Sci. **255**, 68 (2008).
[40] I. Makkonen, E. Korhonen, V. Prozheeva, and F. Tuomisto, J. Phys.: Condens. Matter. **28**, 224002 (2016).
[41] Z. Q. Chen, S. J. Wang, M. Maekawa, A. Kawasuso, H. Naramoto, X. L. Yuan, and T. Sekiguchi, Phys. Rev. B **75**, 245206 (2007).
[42] Z. Q. Chen, S. Yamamoto, M. Maekawa, A. Kawasuso, X. L. Yuan, and T. Sekiguchi, J. Appl. Phys. **94**, 4807 (2003).
[43] A. Uedono, T. Koida, A. Tsukazaki, M. Kawasaki, Z. Q. Chen, S. Chichibu, and H. Koinuma, J. Appl. Phys. **93**, 2481 (2003).
[44] W. Egger, G. Kögel, P. Sperr, and H.-J. Gudladt, Int. J. Mater. Res. **97**, 1633 (2006).
[45] K. M. Johansen, A. Zubiaga, I. Makkonen, F. Tuomisto, P. T. Neuvonen, K. E. Knutsen, E. V. Monakhov, A. Y. Kuznetsov, and B. G. Svensson, Phys. Rev. B **83**, 245208 (2011).
[46] K. M. Johansen, F. Tuomisto, I. Makkonen, and L. Vines, Mater. Sci. Semicond. Proc. **69**, 23 (2017).
[47] F. Lukáč, J. Čížek, I. Procházka, O. Melikhova, W. Anwand, and G. Brauer, Acta. Phys. Pol. A **125**, 748 (2014).
[48] J. Čížek, M. Vlček, P. Hruška, F. Lukác, O. Melikhova, W. Anwand, F. Selim, C. Hugenschmidt, and W. Egger, J. Phys.: Conf. Ser. **791**, 012017 (2017).
[49] F. Linez, I. Makkonen, and F. Tuomisto, Phys. Rev. B **94**, 014103 (2016).
[50] A. Karbowski, K. Fedus, J. Patyk, Ł. Bujak, K. Służewski, and G. Karwasz, Nukleonika **58**, 189 (2013).

[51] S. Lany and A. Zunger, Phys. Rev. Lett. **98**, 045501 (2007).
[52] D. C. Look, in *Zinc Oxide Bulk, Thin Films and Nanostructures*, edited by C. Jagadish and S. J. Pearton (Elsevier, Amsterdam, 2006), p. 37.
[53] H. S. Domingos, J. M. Carlsson, P. D. Bristowe, and B. Hellsing, Interface Sci. **12**, 227 (2004).
[54] R. Ono, T. Togimitsu, and W. Sato, J. Radioanal. Nucl. Chem. **303**, 1223 (2015).
[55] B. Oberdorfer and R. Würschum, Phys. Rev. B **79**, 184103 (2009).
[56] S. Brunner, W. Puff, A. G. Balogh, and P. Mascher, Mater. Sci. Forum **363–365**, 141 (2001).
[57] A. Dupasquier, R. Romero, and A. Somoza, Phys. Rev. B **48**, 9235 (1993).
[58] M. Theelen, K. Polman, M. Tomassini, N. Barreau, H. Steijvers, J. van Berkum, Z. Vroon, and M. Zeman, Surf. Coat. Technol. **252**, 157 (2014).
[59] J. Hüpkes, J. I. Owen, M. Wimmer, F. Ruske, D. Greiner, R. Klenk, U. Zastrow, and J. Hotovy, Thin Solid Films **555**, 48 (2014).
[60] T. Tohsophon, A. Dabirian, S. de Wolf, M. Morales-Masis, and C. Ballif, APL Mater. **3**, 116105 (2015).
[61] N. H. Nickel, Phys. Rev. B **73**, 195204 (2006).
[62] K. Ip, M. E. Overberg, Y. W. Heo, D. P. Norton, S. J. Pearton, C. E. Stutz, S. O. Kucheyev, C. Jagadish, J. S. Williams, B. Luo, F. Ren, D. C. Look, and J. M. Zavada, Solid-State Electron. **47**, 2255 (2003).
[63] J. Čížek, F. Lukáč, M. Vlček, M. Vlach, I. Procházka, F. Traeger, D. Rogalla, H. W. Becker, W. Anwand, G. Brauer, S. Wagner, H. Uchida, A. Pundt, and C. Bähtz, Def. Diff. Forum **333**, 39 (2013).
[64] J. Čížek, N. Žaludová, M. Vlach, S. Daniš, J. Kuriplach, I. Procházka, G. Brauer, W. Anwand, D. Grambole, W. Skorupa, R. Gemma, R. Kirchheim, and A. Pundt, J. Appl. Phys. **103**, 053508 (2008).
[65] W. Beyer, J. Hüpkes, and H. Stiebig, Thin Solid Films **516**, 147 (2007).
[66] See http://www.adem-innovationlab.nl.
[67] M. Geller and E. W. Ng, J. Res. Natl. Bur. Stand. **73B**, 191 (1969).